**Specialized parallel pathways for adaptive control of visual object pursuit**

Matthew F. Collie[1], Chennan Jin[2], Emily Kellogg[1], Quinn X. Vanderbeck[1], Alexandra K. Hartman[1], Stephen L. Holtz[1], and Rachel I. Wilson[1]*
[1]Department of Neurobiology, Harvard Medical School, Boston, MA USA
[2]Present address: Neuroscience Graduate Program, University of California, San Francisco, CA, USA
*Correspondence: rachel_wilson@hms.harvard.edu

## Summary

To pursue an unpredictably moving visual object, the brain must generate motor commands that continuously steer the object to the midline of the visual field via feedback. Behavior implies that visual pursuit relies on a feedback loop with flexible gain, but the mechanisms of this "adaptive control" are not well-understood. Here we show that adaptive control in the *Drosophila* pursuit system involves two parallel feedback loops. One serves to steer the object coarsely toward the midline; the properties of this pathway are relatively constant. The other functions to steer the object precisely to the midline, and its properties are flexible: gain increases when the object is moving away from the midline, when the pursuer is running fast, and during arousal. Genetically suppressing this flexible pathway decreases pursuit performance in aroused males. Our findings show how biological feedback systems can implement adaptive control to drive vigorous error correction while avoiding instability.

**Keywords:** feedback control, object motion, direction selectivity, gain scheduling, steering, in vivo electrophysiology, AOTU019, AOTU025, DNa02

## Introduction

A feedback control system continuously compares its output with some setpoint, and adjusts that output to minimize deviation from the setpoint ("error"). In a basic control system, error simply produces a proportional change in the system's output, with the ratio of output to error is defined as the "gain". Gain can be difficult to optimize: if it is too low, the system under reacts to large errors, leading to sluggish performance, but if the gain is too high, the system overreacts to small errors, producing instability, overshooting, and even oscillations as the system struggles to hold the setpoint[1,2]. The best compromise between these competing constraints can change over time. One solution is adaptive control, where the parameters of a feedback control system are constantly adjusted to match current conditions. For example, the system may adjust its own gain over time ("gain scheduling"), thereby increasing gain when rapid error correction is needed, and reducing gain when stability is more important.

Many animals actually use adaptive control when tracking or pursuing a moving visual object. Such behaviors are widespread in nature, seen in contexts ranging from mate pursuit and territorial defense to prey capture and ocular tracking. In all these situations, pursuit requires feedback—and often involves adaptive control of feedback gain. For example, primates adjust their eye movement pursuit gain depending on the level of attention allocated to the task[2–9]. Dragonflies adjust their pursuit gain depending on both attention[10] and context: they use lower gain when chasing prey but switch to higher gain when chasing other dragonflies, likely because high-gain pursuit leads to overshooting and oscillations that help drive rivals out of their territory[11,12]. Houseflies adjust their pursuit gain during chasing depending on the visual object position on their retina: when the object is far from the midline, gain is fixed, so steering is just proportional to error (i.e. the object's angular distance from the midline). But when the object is close to the midline, gain increases for

objects moving away from the midline, enabling more vigorous corrections[13,14]. However, in all these cases, we know little about the neural mechanisms of such adaptive control.

To investigate these mechanisms, we chose to focus on *Drosophila*, where visual pursuit is particularly prominent during courtship. Specifically, an aroused male will chase a running female until she slows to permit copulation[15,16]. During pursuit, the male's task is to run while orienting toward the female[17–22] – effectively keeping her image aligned with a setpoint at his visual midline (**Fig. 1a**). This is challenging because the female turns unpredictably, requiring the male to make fast compensatory turns to keep up and outmaneuver rival males[23–25]. During pursuit, the image of the moving female (the "visual object" of interest) is encoded primarily by LC10a cells in the optic lobe: these cells are specialized to detect small moving objects, and they are required for pursuit[19,20,26–28]. LC10a cells project to cells in the anterior optic tubercle (AOTU) that also receive inputs signaling the male's arousal state[20,28,29]. Many of these AOTU neurons form the shortest link between visual object motion detection and steering control, synapsing directly onto descending neurons[20,29] that project to locomotor regions of the ventral nerve cord[30–33]. This includes several descending neurons known to influence steering during running[34–37]. However, we do not understand how these different types of AOTU cells transform incoming visual object motion signals into steering commands.

In this study, we show that the pursuit circuit comprises two parallel, functionally distinct AOTU pathways. One pathway detects a moving object far from the midline, and it functions to steer the object back into the midline zone. The other pathway detects a moving object near the midline, and it functions to steer the object precisely to the center of this zone. In this latter pathway, steering commands are more vigorous when the object is moving away from the midline—i.e. when error is increasing. Moreover, the visual gain of the midline pathway increases when the pursuer is running fast, and when the male is sexually aroused. We show that the specializations of the midline pathway are organized to increase the speed of error correction while also avoiding overshooting and wind-up of pursuit errors. Finally, we show that genetically suppressing the midline pathway can measurably decrease pursuit performance. Together, these results show how feedback systems can implement adaptive control via specialized parallel pathways with flexible gain.

## Results

### AOTU circuits divide visual space into parallel pathways

Connectome data[38–41] show that LC10a cells project to steering-related descending neurons (DNs), most notably DNa02[35,36,42], via two major AOTU cell types, called AOTU019 and AOTU025 (**Fig. 1b,c**, **Fig. S1**). LC10a outputs are selective, with each downstream cell receiving input from only a subset of the LC10a population[20]. In particular, we noticed that AOTU019 samples primarily from LC10a cells devoted to the frontal visual field, whereas AOTU025 samples primarily from LC10a cells devoted to the lateral visual field (**Fig. 1d,e**). This anatomy predicts that AOTU019 detects objects near the midline, whereas AOTU025 detects objects farther from the midline.

To test this prediction, we made electrophysiological recordings from AOTU019 and AOTU025 in head-fixed male flies walking on a spherical treadmill (**Fig. 1f**), using split-Gal4 lines we created to target these cells (**Fig. S2a**). We motivated these males to engage in pursuit by optogenetically stimulating P1 cells, as this triggers an increase in male sexual arousal and causes the male to chase any visual object that resembles a female[20,43–48]. To map the visual receptive field of each recorded cell, we presented the fly with a series of isolated small objects on a cylindrical visual panorama. Each object appeared at a random position and then moved in a short rotational path around the fly before disappearing; we refer to these visual stimuli as "motion pulses" (**Fig. 1f**).

As expected, we found that AOTU019 responded best to objects near the midline, whereas AOTU025 responded best to objects farther from the midline (**Fig. 1g,h**).

**Steering can arise from asymmetric excitation or inhibition**

In addition to their receptive field differences, these cells also release different neurotransmitters: AOTU025 is cholinergic, whereas AOTU019 is GABAergic. This conclusion is based on machine classification of electron microscopy images[49], as well as genetic evidence[50] (**Fig. S2b**). This would imply that AOTU025 is excitatory, whereas AOTU019 is inhibitory.

Moreover, AOTU025 projects to the ipsilateral copies of steering DNs, whereas AOTU019 targets the contralateral copies of these DNs (**Fig. 2a, Fig. S3a**). To understand the relevance of this, note that each of these steering DN types is represented by a single pair of mirror-symmetric neurons—one per hemisphere[51]—and when their activity is unequal, the fly turns toward the side of higher DN activity[34–36,42,52] Moreover, the fly's rotational velocity scales with the right-left firing rate difference[35,42]. Therefore, both AOTU cells are predicted to drive turning toward the visual object (**Fig. 2a**). For example, an object on the right will excite both AOTU025 and AOTU019 in the right hemisphere, leading to excitation of right DNs and inhibition of left DNs. Both effects should increase the right-left difference in DN activity, driving rightward turning regardless of which AOTUcell is most active.

To test this prediction, we injected current via the recording electrode into individual AOTU019 or AOTU025 cells, and measured the resulting change in the fly's rotational velocity. We found that direct excitation of either cell type was sufficient to produce ipsilateral turning (i.e., turning toward the side of the excited cell; **Fig. 2b**). Conversely, when we injected hyperpolarizing current to inhibit these cells, we observed contralateral turning (i.e., turning away from the side of the inhibited cell; **Fig. 2b**). The average size of the behavioral response was similar for the two cell types, implying that excitation and inhibition exert similar influence over steering. Together, these results imply that the same rightward rotational velocity can arise through multiple mechanisms—namely, increased excitatory drive to DNs on the right, decreased excitatory drive to DNs on the left, increased inhibitory drive to DNs on the left, decreased inhibitory drive to DNs on the right, or any combination of these. We call this the "see-saw model of steering control"[35] (**Fig. 2c**).

Unexpectedly, we also found that depolarization of AOTU019 significantly increased the male's forward velocity, whereas depolarization of AOTU025 had no effect on forward velocity **Fig. 2b**). This cannot be explained as a direct consequence of faster turning in one group of flies, because the two groups had similar rotational velocity responses (**Fig. 2b)**. These results suggest that AOTU019 can help accelerate the male's forward movement toward a visual object, while also keeping the male oriented toward that object.

Importantly, we can accurately predict the motion pulse responses of steering DNs and the fly's rotational velocity, based on the activity of these two AOTU cells. Here we focused on predicting the activity of DNa02 because this DN strongly correlates with (and influences) steering in walking flies[35,36,42], and it has particularly strong direct and indirect input from AOTU019 and AOTU025 (**Fig. 1c, Fig. S1b**). We used targeted electrophysiological recordings to measure DNa02 responses to motion pulses in male flies that were aroused optogenetically, just as in our AOTU neuron recordings. We found that the combined visually-evoked activity of the four AOTUneurons (AOTU019 and AOTU025, in the right and left hemispheres) could predict the visually-evoked right-left asymmetry in DNa02 activity (**Fig. 2d,e**). We also found that visual responses in DNa02 could predict the fly's rotational velocity in response to motion pulse stimuli (**Fig. 2f, Fig. S4**). While steering is likely influenced by multiple DNs[34–37,42], DNa02 can still be predictive of steering behavior if its visual responses are correlated with those of other co-activated steering DNs. Notably, AOTU019 and

AOTU025 firing rate changes typically precede changes in the fly's rotational velocity (**Fig. 2g**), and they correlate with rotational velocity in a graded manner (**Fig. 2h**).

Taken together, our results thus far imply a clear division of labor in this circuit. AOTU025 detects an object that is far from the visual midline, and it functions to steer the object toward the general vicinity of the midline. Next, AOTU019 detects an object that is in the vicinity of the midline, and it functions to steer the object precisely to the midline, while also increasing the pursuer's forward velocity.

**Direction selectivity is highest around the visual midline**

In principle, pursuit performance would be better if the brain took account of the object's direction of movement. Indeed, we confirmed that the fly's turning behavior is direction-selective, as reported previously[20]: a rightward motion pulse evokes stronger rightward turning, as compared to a leftward pulse in the same retinotopic location (**Fig. 3a**). We discovered that this behavioral bias is stronger for motion pulses near the midline, as compared to more lateral motion pulses, arguing that direction selectivity is strongest around the visual midline.

Moreover, we found that AOTU019 cells are direction-selective: the cell on the right responds best to rightward motion pulses, and vice versa (**Fig. 3b, Fig. S5**). As a result, the interhemispheric difference in AOTU019 firing rate (the right cell - left cell difference) is larger when an object is moving away from the midline, as compared to an object moving toward the midline (**Fig. 3b,c**). LC10a cells on the right are also preferentially responsive to rightward motion pulse[19,20]. By comparison, we found that AOTU025 is significantly less direction-selective than AOTU019 (**Fig. 3b,c, Fig. S5**).

To show why direction selectivity is particularly useful around the midline, we can use our network model (**Fig. 2a**) to simulate a fly's pursuit of a visual object (**Fig. 3d**). In this simulation, the pursuer maintains a fixed distance from the object, and we assess how well the pursuer can reorient to face the object by tracking the object's movement across the visual field. At each time point, the object's position on the pursuer's retina is used to model the visual responses of AOTU019 and AOTU025, based on our data (**Fig 1e,h**). The combined activity of these AOTU cells generates the pursuer's predicted steering signal, which in turn updates the object's position on the retina via feedback. This simulation illustrates the basic point that lateralized excitation (from AOTU025) and inhibition (from AOTU019) can work together to produce smooth, object-directed steering commands, and this tends to bring the object toward the visual midline even if the visual system is not direction-selective (**Fig. 3e**). Adding direction selectivity to AOTU019 improves pursuit performance: the object is maintained closer to the visual midline (**Fig. 3e**), and the system restabilizes more quickly after abrupt object movements (**Fig. 3f**). By contrast, when we add direction selectivity to AOTU025, the benefit is negligible (**Fig. 3e,f**). This is because a large error (i.e., a large object distance from the midline) demands a rapid corrective turn regardless of the object's direction of motion. This may explain why it is useful for AOTU019 to be more direction-selective than AOTU025.

Direction selectivity in this circuit can be understood as a form of adaptive control in steering gain. Recall that gain is the ratio of output (steering) to error (object distance from the midline). In effect, direction selectivity in AOTU019 increases steering gain when the object is near the midline but moving away from it–when error is small but increasing. Conversely, this allows steering gain to be lower when error is small and decreasing[53–55], so that the system does not risk overshooting. As overshooting is only a problem near the midline, it makes sense that direction selectivity would be particularly important in the pathway devoted to detecting a visual object near the midline.

**Faster running increases steering and visual responses near the midline**

During courtship, males vary not only their steering, but also their forward velocity[17,19]. This raises the question of how steering and forward movement are coupled during pursuit behavior. To investigate this issue, we placed an optogenetically aroused male in a virtual reality environment where he could freely orient toward a moving visual object (**Fig. 4a**), without coming closer to it. This paradigm allows the male to pursue the object with variable vigor over time. We found that epochs of more consistent orienting toward the object typically occurred when the male was also running faster forward (**Fig. 4b**). Moreover, a given visual object position on the male's front visual field evoked stronger steering responses when the male's forward velocity was also high (**Fig. 4c**). In particular, the ratio of rotational velocity to object position ("steering gain") was significantly larger when the male was running forward fast (**Fig. 4d**).

This link makes sense: increased steering and increased forward velocity both bring the male closer to the female. Moreover, precise steering becomes more important at higher forward velocity, because any angular error produces a faster-growing deviation between the male and the female path (i.e., there is faster "wind up" of angular error into translational error; **Fig. 4e**). For both these reasons, it is logical that increases in forward velocity are associated with increased steering gain.

Next, we asked whether spontaneous increases in the male's forward velocity are associated with increases in AOTU visual responses. Here, we focused on our motion pulse experiments, where the visual stimulus is independent of the fly's behavior. We found that AOTU responses increased with forward velocity, and this effect was graded and nearly linear (**Fig. 4f**). However, this relationship was significantly steeper for AOTU019, as compared to AOTU025.

Moreover, when the male was running faster, motion pulses produced larger interhemispheric differences in AOTU019 activity (**Fig. 4g,h**). For example, when the object is on the right and the male is running faster, this should produce higher rightward rotational velocity and, consequently, greater steering gain toward the object. During fast running, we found no significant interhemispheric differences in AOTU025 activity (**Fig. 4g,h**), suggesting that AOTU025 does not contribute to higher steering gain.

To summarize, increased forward velocity is correlated with increased steering gain, stronger visual responses in AOTU019, and increased interhemispheric difference in AOTU019 activity. So what is the causal relationship here? On one hand, AOTU019 firing rate fluctuations are essentially synchronous with changes in forward velocity (peak cross-correlation lag = –3.00 ± 8.46 ms, n = 25 recordings), suggesting that changes in forward velocity are initiated by other pathways, with AOTU019 receiving a copy of these motor commands. In this regard, it is notable that AOTU019 has a large dendritic arbor in the lateral accessory lobe (LAL; a premotor brain region) whereas AOTU025 does not (**Fig. 2a**, **Fig. S3a,b**). At the same time, direct depolarization of AOTU019 can drive increases in forward velocity (**Fig. 2b**). Together, these findings support a model in which a forward velocity command boosts AOTU019 visual responses, thereby increasing steering gain and reinforcing the drive to run forward—provided the visual object remains near the midline.

**Arousal recruits the pathway for detecting objects near the midline**

Until now, we have focused on epochs in which males were motivated to engage in pursuit by optogenetically stimulating P1 cells. Given our findings that AOTU019 is a locus of adaptive control, we asked whether P1 cell stimulation might preferentially increase the relative contribution of AOTU019 cells. Indeed, we found that arousal (resulting from P1 optogenetic stimulation) produced a large depolarization and a large increase in firing rate in AOTU019 cells (**Fig. 5a,b**). By comparison, arousal produced a smaller depolarization and a

smaller increase in firing rate in AOTU025 cells (**Fig. 5a,b**). Arousal also increased the magnitude of the visually-evoked change in firing rate in both cell types, as it does in LC10a cells[20], but this effect was larger in AOTU019 than AOTU025 (**Fig. 5c**). As a control, we confirmed that arousal induced a similar increase in running behavior in both recording groups (**Fig. 5d**). Together, these results show that arousal increases activity in both cell types, but it particularly increases the contribution of AOTU019.

Arousal causes these males to orient more accurately toward a visual object (**Fig. 5e**), and it also increases the amount of time spent in the pursuit state (defined as epochs of sustained running while orienting toward the object; **Fig. 5f**). Recruitment of AOTU019 is likely important in promoting accurate visual orientation, for three key reasons: its receptive field focuses on the visual midline (**Fig. 1**), its direction selectivity should reduce overshooting (**Fig. 3**), and its contribution increases during fast forward running (**Fig. 4**).

**Suppressing the pathway for detecting objects near the midline impairs pursuit**

If AOTU019 is indeed important in promoting accurate visual orientation, then suppressing AOTU019 in aroused males should decrease steering toward a visual object. To test this idea, we generated flies that expressed the inwardly rectifying potassium channel Kir2.1 in AOTU019 cells under split-Gal4/UAS control (**Fig. S6a,b**), and we compared these flies to two genetic controls: one bearing only the UAS-Kir2.1 transgene, and the other bearing only the AOTU019 split-Gal4 line. In all three genotypes, P1 cells were stimulated to produce arousal (**Fig. 6a**). As before, we placed each aroused male in a virtual reality environment where he could freely orient toward a moving visual object, without coming closer to it (**Fig 4a**). We found that suppressing AOTU019 activity produced a significant decrease in the male's steering toward the visual object during pursuit (**Fig. 6b,c**). We confirmed that this steering defect was not attributable to a generalized locomotor defect: there was no effect on the probability of pursuit engagement (**Fig. 6a**) or optomotor turn responses (**Fig. S6c,d**). The size of the steering defect was small, but this is consistent with the predictions of our network model. In this model, if we eliminate AOTU019 entirely, the male still tends to bring the object toward his visual midline, but the male does not correct small pursuit errors as quickly as it does otherwise (**Fig. 6d**). The small effect of removing AOTU019 in this model is quantitatively similar to the phenotype observed when we genetically suppress AOTU019 (**Fig. 6b,c**), provided that the model includes the additional minor AOTU cells in the connectome. These minor AOTU have predicted visual receptive fields that overlap with those of AOTU019 and AOTU025 (**Fig. S7**), and although they form relatively weak anatomical pathways from LC10a cells to steering DNs (**Fig 1c**), their collective contributions can help explain why steering around the midline does not disappear completely when AOTU019 is suppressed.

Interestingly, suppressing AOTU019 did not reduce the male's overall forward velocity (**Fig. 6e**) or his tendency to run faster when oriented toward the object during pursuit (**Fig. S6f**), consistent with the idea that spontaneous forward velocity fluctuations are driven by other pathways. However, because males tend to orient toward the object more precisely at higher speeds (**Fig. 4b**), it is difficult to assess how AOTU019 activity affects visually evoked forward acceleration in an experimental design where the male has control of the object's position in his visual field. We therefore presented the male with an object oscillating back and forth across the visual field, where the object position was not dependent on the male's behavior (**Fig. S6c**). Males showed a reliable forward acceleration as the object crossed the midline, and this response was significantly blunted by suppressing AOTU019 (**Fig. 6f**). This reveals a contribution of AOTU019 to visually driven forward acceleration that is only detectable when visual input is decoupled from behavior.

**Discussion**

---

Behavioral studies have shown that visual object pursuit involves adaptive control—the continuous

adjustment of control system parameters to suit current conditions[2,4–6,11,13,56–64]. In this study, we investigated mechanisms of adaptive control in the *Drosophila* pursuit system. We focused on the two major parallel pathways (AOTU019 and AOTU025) that link object detectors (LC10a cells) with steering DNs. We found that both AOTU cells drive steering toward a visual object; however, AOTU019 specifically detects objects close to the midline, whereas AOTU025 detects objects farther from the midline. Our results imply that AOTU025 functions to steer the object toward the general vicinity of the midline, while AOTU019 specializes in steering the object precisely to the midline.

Our results are interesting from a motor systems perspective, because they provide a clear example of how an increase in synaptic inhibition can actually initiate a downstream motor program: although AOTU019 is inhibitory, it is as potent in driving steering as AOTU025 is. In reality, these two AOTU pathways are probably co-activated much of the time, given that their visual receptive fields overlap. Thus, steering toward a visual object is probably often guided by a combination of ipsilateral excitation and contralateral inhibition. Similarly, there is anatomical evidence that other pathways also guide steering using this type of "see-saw" strategy[35]. In visual circuits, this motif is known as "crossover inhibition", and it may have a general function in reducing the impact of global drifts or perturbations in neural activity[65].

Notably, we found that the AOTU019 pathway is direction-selective: this pathway generates a stronger steering drive when an object is moving away from the midline. By comparison, AOTU025 is less direction-selective. This feature of AOTU019 helps explain a key aspect of the behavior: male steering during pursuit depends on the object's direction of motion only when the object is near the midline. Direction selectivity near the midline is useful because it helps prevent overshooting and oscillations – issues that are less of a concern when the object is farther from the midline. Interestingly, work in other insect species has also found evidence that pursuit is only sensitive to the direction of object motion in a limited part of the pursuer's visual field[13,14,66–68].

Intuitively, direction selectivity allows the steering system to anticipate the future position of the visual object, thereby reducing the effective delay between visual signals and behavioral responses. In the language of control theory, the direction selectivity of AOTU019 can be seen as adding a derivative control term to the steering system. To make this explicit: we define the object positional deviation from the midline as the error ($\varepsilon$), and object direction as the sign of $dt/d\varepsilon$; thus, direction selectivity in AOTU019 means this cell is sensitive to $dt/d\varepsilon$ (and not just $\varepsilon$). Engineered feedback systems are often designed to increase output when error is growing ($dt/d\varepsilon > 0$) and to decrease output when error is shrinking ($dt/d\varepsilon < 0$), because this dependence on $dt/d\varepsilon$ can reduce instability[69]. As an aside, we found that AOTU019 cells are sensitive to the direction of the object but not its speed (**Fig. S8**), like LC10 cells[19]. In the vertebrate retina, some ganglion cells have this property of being direction selective but speed-invariant[53–55]. Speed-invariance in the primate smooth ocular pursuit system is thought to help reduce over-corrections in response to the higher frequency component of object motion[2], and the same may be true of AOTU019.

Another specialization of the midline-steering pathway is its sensitivity to forward velocity. Higher forward velocity increases steering drive in AOTU019 cells, and this can help explain why the male turns more vigorously when he is running forward fast. This modulation can be seen as a form of adaptive control: when the male fly is running fast, any lingering error in his orientation toward the female can rapidly increase the translational distance between them, diminishing the male's chances of reproductive success in a competitive environment[23]. By scaling steering gain with forward velocity, the system also allows for lower gain at slow speeds, potentially conserving energy and reducing the risk of instability associated with excessive gain..

Our data imply that AOTU019 is not required to initiate forward acceleration; rather, forward velocity commands are likely "copied" onto AOTU019, potentially through this cell's dendrites in premotor brain regions (**Fig. 2a**, **Fig. S3a,b**). Nonetheless, activating AOTU019 can increase forward velocity (**Fig. 2b**) an effect that may be mediated, at least in part, by inhibition of "moonwalker DNs", which arrest forward velocity[70], and inhibiting these DNs may release a brake on forward running. This would create a potential positive feedback loop: an outgoing forward velocity command increases AOTU019 activity, which increases the steering drive to keep the object near the midline and further promotes the ongoing drive to run forward. This positive feedback loop should sustain AOTU019 activity and may contribute to the persistence of pursuit behavior once courtship is initiated[71,72].

We found that arousal increases activity in both AOTU pathways, but this effect is significantly larger in AOTU019. This suggests that AOTU019 is preferentially recruited when higher performance is needed. Many animals exhibit high performance behavior in specific goal-oriented contexts. For example, larval zebrafish make more precise eye movements while hunting[73], due to the recruitment of additional motor neurons[74]. Flies execute a more precise takeoff maneuver if time is available, by selecting one of two available parallel neural pathways for takeoff[75]. In the fly visual pursuit system, sexually dimorphic arousal neurons are dynamically recruited during both male courtship (e.g., P1 neurons[20,43–48]) and female aggression (e.g., aIPg neurons[28,29]) to gate visual processing during social interactions. While this study focuses on general principles of adaptive control in male flies, it is important to recognize that the same pathways exist in females, and these female-specific arousal neurons connect more strongly to AOTU019 than to AOTU025[29]. With the advent of a male brain connectome, future work will be well-positioned to directly compare this circuit across sexes.

Finally, we show that suppressing AOTU019 activity in aroused males decreases steering in the direction of the visual object, while also decreasing male's tendency to accelerate forward when the visual object is near the midline of his visual field. These results support the conclusion that AOTU019 functions to increase the precision of object-directed steering, while also amplifying the male's tendency to run faster when the object is directly ahead. It is perhaps surprising that suppressing AOTU019 has any phenotype: although LC10a cells are necessary for turning towards a visual object during courtship pursuit[19,20], there is only one AOTU019 cell in each hemisphere, and this is only one of 14 cells postsynaptic to LC10a and presynaptic to DNa02[20] (**Fig. 1c, Fig. S1**).

Our work raises several questions for future work. For example, AOTU019 has a remarkably thick cable diameter (**Fig. S3b,c**), which suggests a specialization for fast processing speed. Fast processing may be particularly important in flight, as AOTU019 makes strong anatomical connections onto some flight-steering-DNs[30,51,52](**Fig. S1c**). As we learn more about the functional specializations of different steering DNs — in flight and in walking[30,34–37,42,51,52,76–79] — it will be interesting to investigate why only a subset of steering DNs are under the control of AOTU019 and AOTU025. In dragonflies, visual pursuit during flight is mediated by an ensemble of DNs with distinct but overlapping visual receptive fields[68,80,81], suggesting that different DNs are recruited at different times. In this way, visual objects in different locations around the body could elicit distinct combinations of rotational and translational movements. Finally, it seems likely that AOTU019 and AOTU025 receive nonvisual inputs as well as visual inputs, and so they may play a more general role in steering, outside the context of visual object pursuit (**Fig. S9**). For instance, AOTU019 is directly downstream from central complex output neurons[82,83] and thus may also contribute to precise error corrections during central complex–mediated navigation.

In summary, our work illustrates two strategies for implementing adaptive control in a biological feedback system. The first strategy is to create two or more parallel pathways inside a feedback loop, with different

gains or control rules in each pathway. Then, as conditions change, signals can dynamically engage different pathways. For example, in the pursuit system, we show that visual signals increasingly engage AOTU019 over AOTU025 as an object approaches the midline. The second strategy is to use an internal state variable to adjust a control parameter. For example, in the pursuit system, our data suggest that forward acceleration commands and arousal states are used to adjust steering gain, particularly near the midline. Together, these strategies allow the system to implement different control rules in different conditions, effectively deconstraining the system and increasing its robustness.

**Resource availability**

**Lead contact:** Requests for further information and resources should be directed to and will be fulfilled by the lead contact, Rachel Wilson (rachel_wilson@hms.harvard.edu).

**Materials availability:** This study did not generate new unique reagents.

**Data and code availability:** All data reported in this paper will be shared by the lead contact upon request. This paper does not report original code.

**Acknowledgements**

We thank F. Loesche, M. Reiser, O. Mazor, and P. Gorelik for their assistance with the visual panorama systems; H. Yang for sharing data acquisition and analysis code; A. Bates for cable width calculations; and the Wilson Lab members for their feedback. We thank the Princeton FlyWire team and consortium (supported by BRAIN Initiative grants MH117815 and NS126935 to Murthy and Seung) for sharing the connectomes and relevant neuron proofreading and annotation. This research was supported by the Harvard Medical School Research Instrumentation Core (NEI P30 Core Grant for Vision Research EY012196) and the Neurobiology Imaging Facility. Funding was provided by NSF GRFP grant DGE2140743 (to M.F.C.), NIH F31 grant 1F31NS130782 (to M.F.C.), and NIH U19 grant U19NS104655 (to R.I.W.). M.F.C. was a Stuart H.Q. & Victoria Quan Fellow at Harvard Medical School, and R.I.W. is an HHMI Investigator.

**Author contributions**

M.F.C. and R.I.W. designed the study. M.F.C. performed electrophysiology experiments, generated the models, and analyzed the data. M.F.C. and C.J. conducted behavioral genetics experiments. C.J. and E.K. generated and described the driver lines used in this study. Q.X.V. proofread neurons in the FAFB EM dataset. A.K.M. contributed to pilot experiments, and S.L.H. provided technical support. M.F.C. and R.I.W. wrote the manuscript.

**Declaration of interests**

The authors declare no competing interests.

**Supplemental information**

Document S1. Figures S1–S9 and Table S1

**Highlights**

- Parallel pathways detect a visual object in the frontal versus lateral visual field
- Steering arises from combined ipsilateral excitation and contralateral inhibition
- The circuit for frontal objects is direction-selective, for anticipatory steering
- The circuit for frontal objects is also recruited during fast running and arousal

**eTOC blurb**

Collie et al. show that the *Drosophila* visual pursuit circuit consists of two parallel feedback pathways through the AOTU: one provides constant gain for coarse steering, while the other adaptively boosts gain for precise midline correction. This architecture supports vigorous, state-dependent pursuit while maintaining feedback stability.

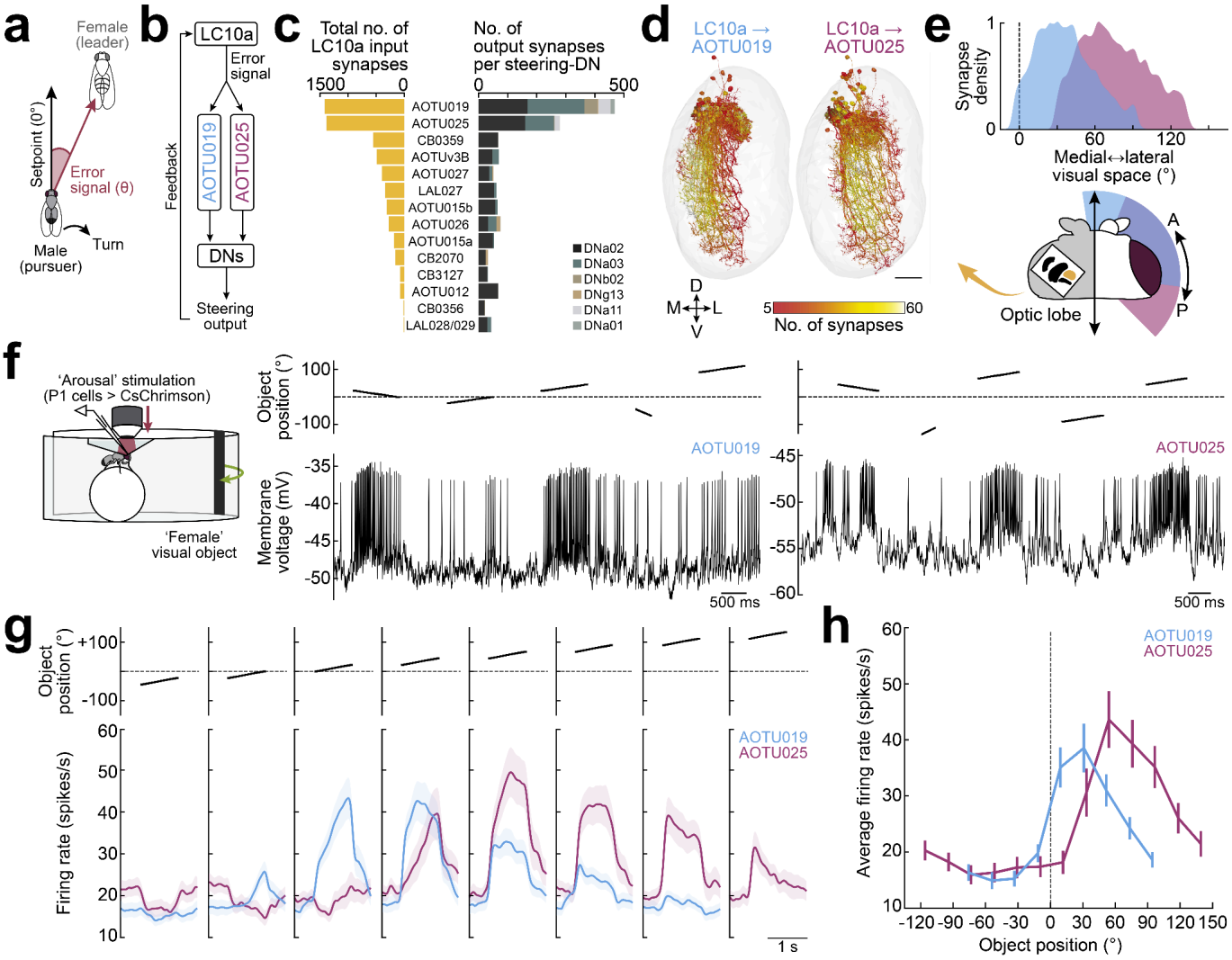


**Figure 1: Visual space is divided into overlapping parallel AOTU pathways.**

**a**, Schematic of male ("pursuer") and female ("leader") during pursuit. Deviation of the female from the male's visual midline (0°) defines an angular error signal (θ), which drives a corrective turn to reduce the discrepancy between current output and the setpoint.

**b**, Proposed feedback control model of visual object pursuit in *Drosophila*. LC10a cells detect a moving visual object and influence steering descending neurons (DNs) largely via AOTU019 and AOTU025.

**c**, Total number of LC10a input synapses and output synapses per identified steering-related DN (averaged across hemispheres), shown for all AOTU cells that both receive input from LC10a and project to DNa02. Relevant DNs included: DNa01[35,42], DNa02[35,42], DNa03[36], DNa11[36], DNb02[37], and DNg13[42]. DNa03 is unusual in that most of its outputs are within the central brain, forming strong connections onto other DNs such as DNa02[36] (**Fig. S1b**). AOTU019 and AOTU025 form the strongest LC10a-to-DN pathway. All connectome analyses use FAFB/FlyWire data[38–40,84,85].

**d**, LC10a cell dendritic arbors in the lobula (LO), color-coded by synapse count onto AOTU019 and AOTU025. Scale bar: 20 µm.

**e**, Visual receptive field estimates of AOTU019 and AOTU025 projected onto LO (top panel) and retinal (bottom panel) coordinates, including 15° binocular overlap[86,87]. The LO (yellow optic lobe structure) medial-lateral axis maps onto the retina's anterior-posterior axis, suggesting AOTU019 is tuned to objects near the midline (anterior) and AOTU025 is tuned to objects more laterally (posterior).

**f**, Schematic of the male fly-on-ball setup showing patch-clamp recording, motion of a visual object across the panoramic display, and P1 activation via CsChrimson. Right: Example recordings from right AOTU019 and AOTU025 during motion pulses at 25 and 75 °/s. Motion stimuli spanned the front 100° for AOTU019 and 180° for AOTU025, with all pulses traversing 22.5° of azimuth.

**g**, Visual responses to repeated motion pulses for AOTU019 (mean ± s.e.m., n = 25 flies) and AOTU025 (n = 22 flies). Cells in the right hemisphere were shown rightward motion pulses, while cells in the left hemisphere were shown leftward motion pulses. Data from the left hemisphere is mirrored and combined with right-hemisphere data for panels (g,h). Response latencies: 39.98 ± 8.46 ms (AOTU019) and 35.88 ± 9.52 ms (AOTU025).

**h**, Average firing rate during each motion pulse presentation, plotted at the center of each sweep position, for AOTU019 (mean ± s.e.m., n = 25 flies) and AOTU025 (n = 22 flies).

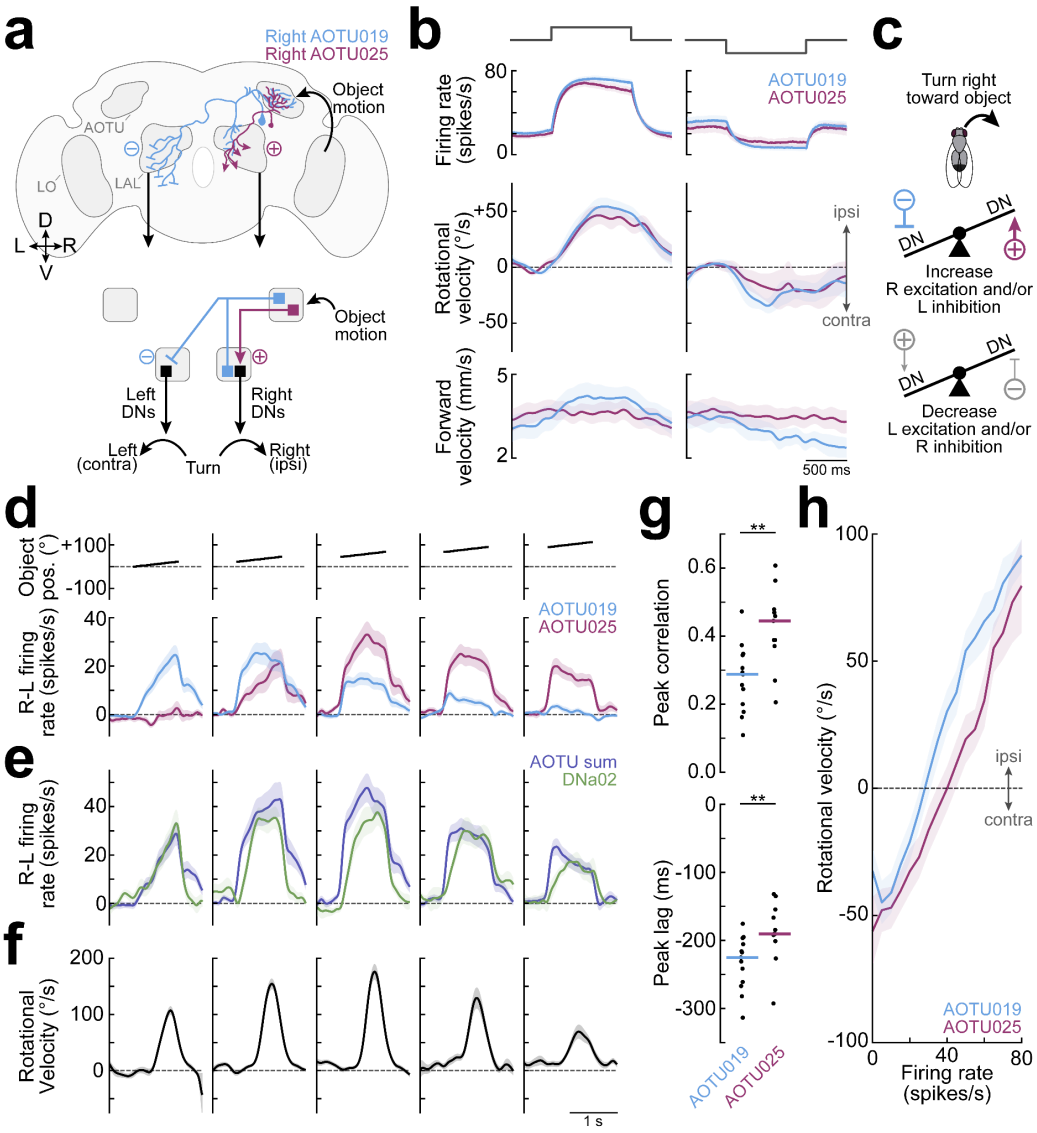


**Figure 2: Steering can arise from asymmetric excitation or inhibition.**

**a**, Frontal schematic of the fly brain (top) and simplified circuit diagram (bottom). AOTU019 and AOTU025 link visual object motion—via LC10a inputs from the LO—to steering-related descending neurons (e.g., DNa02) in premotor regions such as the lateral accessory lobe (LAL). AOTU019 is inhibitory and contralateral, with dendritic compartments (squares) in both the AOTU and LAL. In contrast, AOTU025 is excitatory and ipsilateral, with dendrites restricted to the AOTU. A "cell on the right" refers to a neuron whose soma and dendrites reside on the right hemisphere of the brain. Detailed morphologies of AOTU cells are shown in **Fig. S3a**.

**b**, Changes in firing rate and behavior (mean ± s.e.m. across flies) caused by positive and negative current injection into AOTU019 (+: n = 15 flies; −: n = 8 flies) and AOTU025 (+: n = 15 flies; −: n = 5 flies). Depolarization drove ipsilateral turning ($p < 0.0001$ for either cell type), while also increasing forward velocity for AOTU019 ($p < 0.005$). Hyperpolarization of AOTU019 drove contralateral turning ($p < 0.05$), with a trend toward reduced forward velocity ($p = 0.066$). Hyperpolarization of AOTU025 did not significantly affect rotational velocity ($p = 0.362$), and there was no significant effect on forward velocity for AOTU025 ($p = 0.246$). Ipsilateral means toward the recorded soma: thus, depolarizing either soma on the right produces rightward turning.

**c**, Schematic of see-saw steering control via AOTU inputs. Steering can result from asymmetric excitation or inhibition: increasing excitation to the right, decreasing excitation to the left, increasing inhibition to the left, or decreasing inhibition to the right. These mechanisms may act alone or in combination.

**d**, Blue: motion pulse responses of AOTU019 cells on the right, minus responses of AOTU019 in the left hemisphere (mean ± s.e.m., n = 23 flies), for objects moving rightward. Magenta: same for AOTU025 (n = 22 flies). Responses were recorded during P1 optostimulation. Data from right and left hemispheres were combined under the assumption of mirror symmetry (see Methods).

**e**, Green: responses of DNa02 on the right, minus responses of DNa02 on the left (mean ± s.e.m., n = 11 flies). Purple: sum of AOTU019 and AOTU025 responses from (c), mean ± s.e.m. with error propagation.

**f**, Turn responses to rightward motion pulses (mean ± s.e.m., n = 40 flies).

**g**, Peak cross-correlation between firing rate and rotational velocity during motion pulse presentation for AOTU019 (n = 13 flies) and AOTU025 (n = 11 flies). Negative lag indicates firing precedes turning. Both cells precede steering, although AOTU025 has a stronger correlation ($p < 0.01$) and shorter lag ($p < 0.01$). Horizontal lines indicate medians.

**h**, Mean rotational velocity (± s.e.m.) binned by cell firing rate 200 ms in the past, measured during motion pulse presentation, for AOTU019 (n = 13 flies) and AOTU025 (n = 11 flies). No significant difference was observed between cell types ($p = 0.156$).

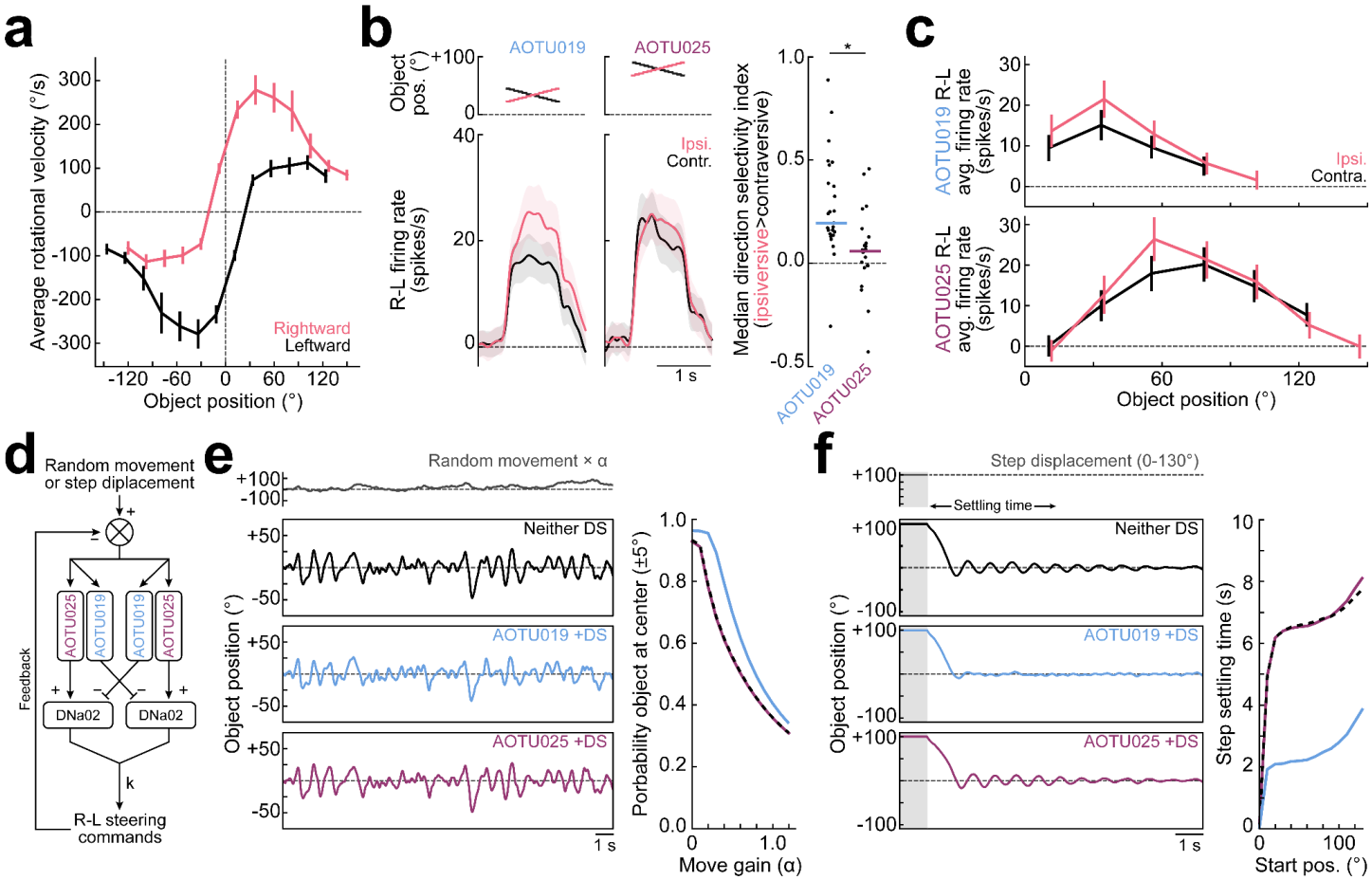


**Figure 3: Direction selectivity is highest around the frontal visual field.**

**a**, Turn responses to 25 °/s motion pulses moving rightward or leftward in head-closed males (mean ± s.e.m., n = 16 flies). In general, flies turned toward the object's position (e.g., rightward turns for stimuli on the right), with a notable exception near the midline, where flies instead tended to follow the direction of motion. Turn responses differed significantly depending on both sweep position and motion direction ($p < 0.0001$, interaction).

**b**, Example visual responses (R-L) to motion pulses at each cell's preferred object position for leftward sweeps, shown for right AOTU019 (mean ± s.e.m., n=25 flies) and AOTU025 (n=22 flies). Right: Median direction selectivity index (DSI) calculated across sweep positions that evoked measurable visual responses. Positive DSI values indicate a preference for ipsiversive motion. AOTU019 was, on average, significantly more direction selective than AOTU025 for sweeps moving at 25 °/s ($p < 0.05$). Analyses during stationary epochs shown in **Fig. S5**. Horizontal lines indicate medians.

**c**, Right-left visual response means (± s.e.m.) to motion pulses moving in the ipsiversive or contraversive direction for AOTU019 (n = 25 flies) and AOTU025 (n = 22 flies). AOTU019 responses showed a significant difference between motion directions ($p < 0.05$), whereas AOTU025 responses did not ($p = 0.6674$). Both AOTU019 ($p = 0.1903$) and AOTU025 ($p = 0.0814$) showed a trend toward greater direction selectivity at more medial compared to lateral positions, as indicated by the interaction term.

**d**, Dynamic simulation of pursuit steering behavior based on LC10a-predicted receptive fields for AOTU019 and AOTU025. Visual inputs are weighted by output strength onto DNa02 and following a 200 ms delay (**Fig. 2g**). Right-left difference in DNa02 activity produces the steering command, scaled by gain parameter *k* (1.2×). The circled "X" indicates where object motion at each time step is compared with steering feedback. For the random object trajectory (simulating female movement), we varied the magnitude (α) of the object's independent movement. For the step displacement, we varied the size of the initial object displacement (0-130°).

**e,** Example simulations using a random object trajectory (α = 0.7; see Methods), showing that the feedback system drives the object toward the midline (0°). Right: Adding direction selectivity to AOTU019 (0.7 penalty to object motion in the contraversive direction) improves pursuit performance, whereas applying the same manipulation to AOTU025 does not, with performance overlapping with the neither-direction-selective condition.

**f,** Example simulations using a step response. The object was held at 100° for 1 s to reach steady-state (gray shading) before release; "settling time" was defined as the time for the object to remain within a ±2° tolerance band for > 1 s. Right: Adding direction selectivity (0.7) to AOTU019 reduces settling time, whereas applying the same manipulation to AOTU025 does not.

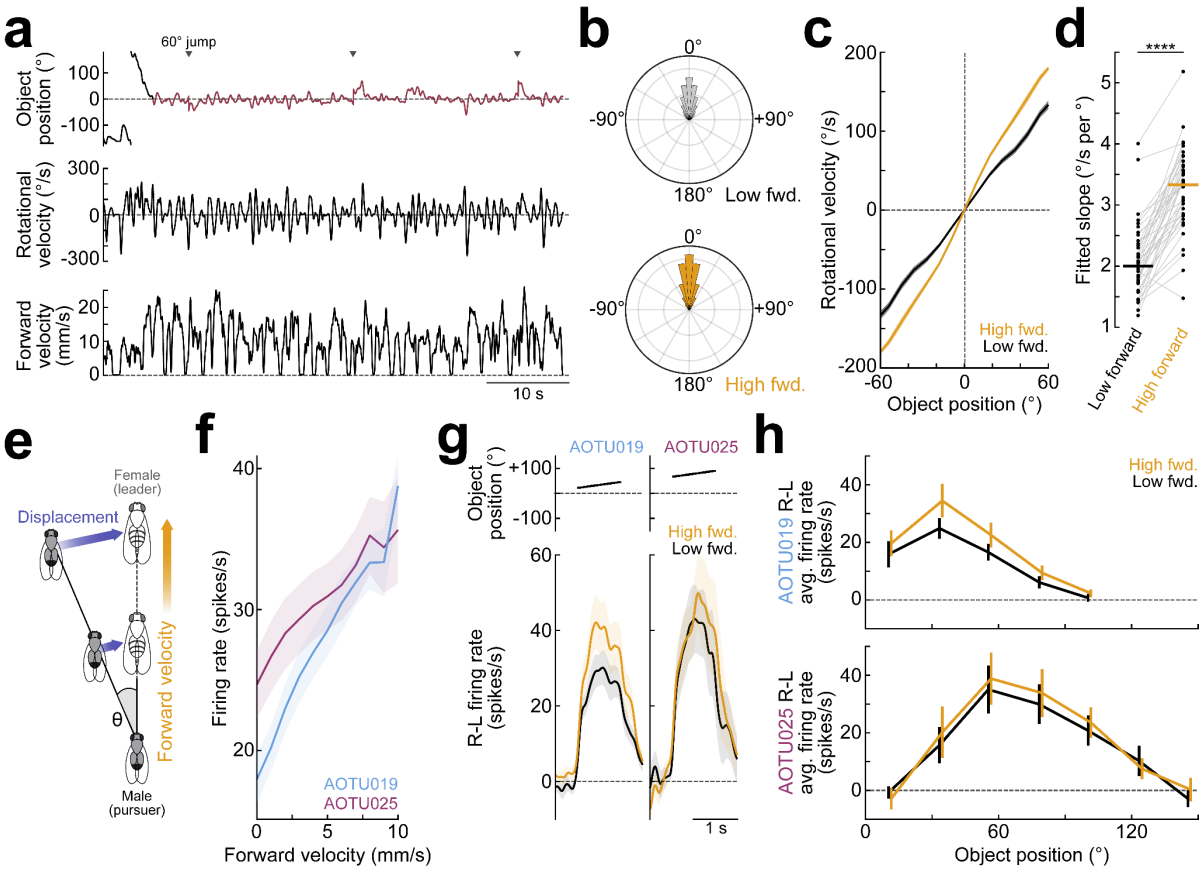


**Figure 4: Increasing forward velocity increases steering gain.**

**a**, Example of an arousal-stimulated male pursuing a virtual "female" in closed-loop with his own rotational velocity. Green trace indicates behavior classified as pursuit. Triangles indicate ±60° object "jumps," used to sample a wider range of virtual female positions and to evoke compensatory turns during pursuit.

**b**, Polar histogram showing the distribution of visual object positions during pursuit for low (bottom third) and high (top third) forward velocity epochs (n = 40 flies). Data are shown as probability density (range: 0-0.2).

**c**, Rotational velocity during pursuit, binned by virtual female position in the front field of view (<60°), for low (bottom third) and high (top third) forward velocity epochs (mean ± s.e.m., n = 40 flies).

**d,** Higher forward velocity is associated with significantly greater steering gain, where gain is the fitted slope of the relationship between rotational velocity and object position (n = 40 flies, $p < 0.0001$). Horizontal lines indicate medians.

**e**, Schematic depicting how the same angular error (θ) will lead to a larger displacement from the male (pursuer) to the female (leader) as forward velocity increases, requiring larger corrective turns at faster speeds.

**f**, Firing rate binned by forward velocity, measured during motion pulse presentation, for AOTU019 (mean ± s.e.m.; n = 25 flies) and AOTU025 (n = 20 flies). Changes in AOTU019 firing were typically synchronous with changes in forward velocity (median ± s.e.m.; –3.00 ± 8.46 ms), whereas most AOTU025 cells lacked a clear cross-correlation lag, reflecting a more binary relationship with movement. Cell types differed significantly ($p < 0.05$), with spiking varying by velocity in a cell type–specific manner (interaction, $p < 0.0001$).

**g,** Visual responses to motion pulses at each cell's preferred object position during low (<median) and high (>median) forward velocity epochs for AOTU019 (mean ± s.e.m., n = 15 flies) and AOTU025 (n = 8 flies).

**h**, Right-left visual response means (± s.e.m.) to motion pulses during low (<median) and high (>median) forward velocity epochs for AOTU019 (n = 15 flies) and AOTU025 (n = 8 flies). Higher forward velocity significantly changes the right-left visual response in AOTU019 ($p < 0.01$), but not AOTU025 ($p = 0.768$).

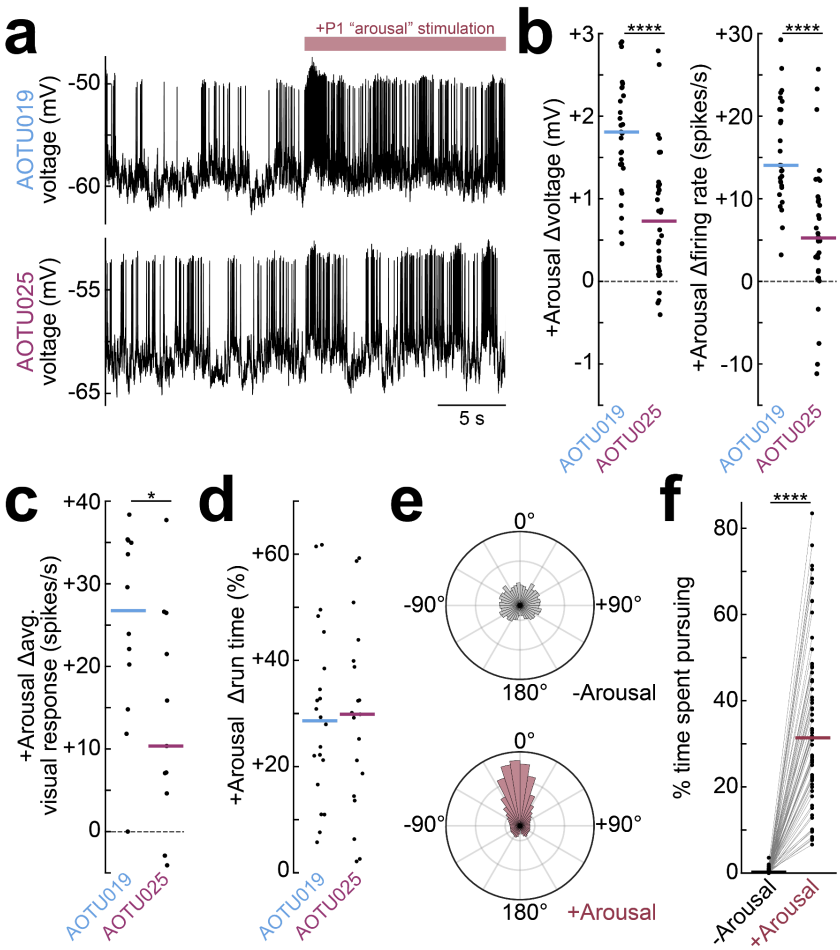


**Figure 5: Arousal preferentially recruits the pathway for detecting frontal objects.**

**a**, Example recordings from right AOTU019 and AOTU025 before and during arousal stimulation via P1 optogenetic activation, recorded while the fly walked in darkness.

**b**, Change in membrane voltage and firing rate for AOTU019 (n = 31 flies) and AOTU025 (n = 34 flies), measured during stationary epochs, following arousal stimulation via P1 optogenetic activation. AOTU019 showed a significantly larger increase in activity than AOTU025 ($p < 0.0001$). Note, the 250 ms immediately after activation onset/offset were excluded from analyses. Horizontal lines indicate medians.

**c**, Change in average visual response, measured at each cell's preferred object position during stationary epochs, for AOTU019 (n = 12 flies) and AOTU025 (n = 11 flies) following arousal stimulation. AOTU019 showed a significantly larger increase in visual response than AOTU025 ($p < 0.05$).

**d**, Percentage of time spent running before and after arousal stimulation in darkness for AOTU019 (n = 22 flies) and AOTU025 (n = 19 flies). No significant difference between groups ($p = 0.971$).

**e**, Polar histogram showing the distribution of visual object positions for males pursuing a virtual "female" in closed-loop with their own rotational velocity following arousal stimulation (n = 61 flies). Data are shown as probability density (range: 0-0.1). During arousal, males concentrated the object near the visual midline (0±30°), whereas pre-arousal object positions were more widely distributed.

**f**, Percentage of time male spent pursuing a virtual "female" before and during arousal stimulation (n = 61 flies). P1 stimulation significantly increased pursuit behavior ($p < 0.0001$).

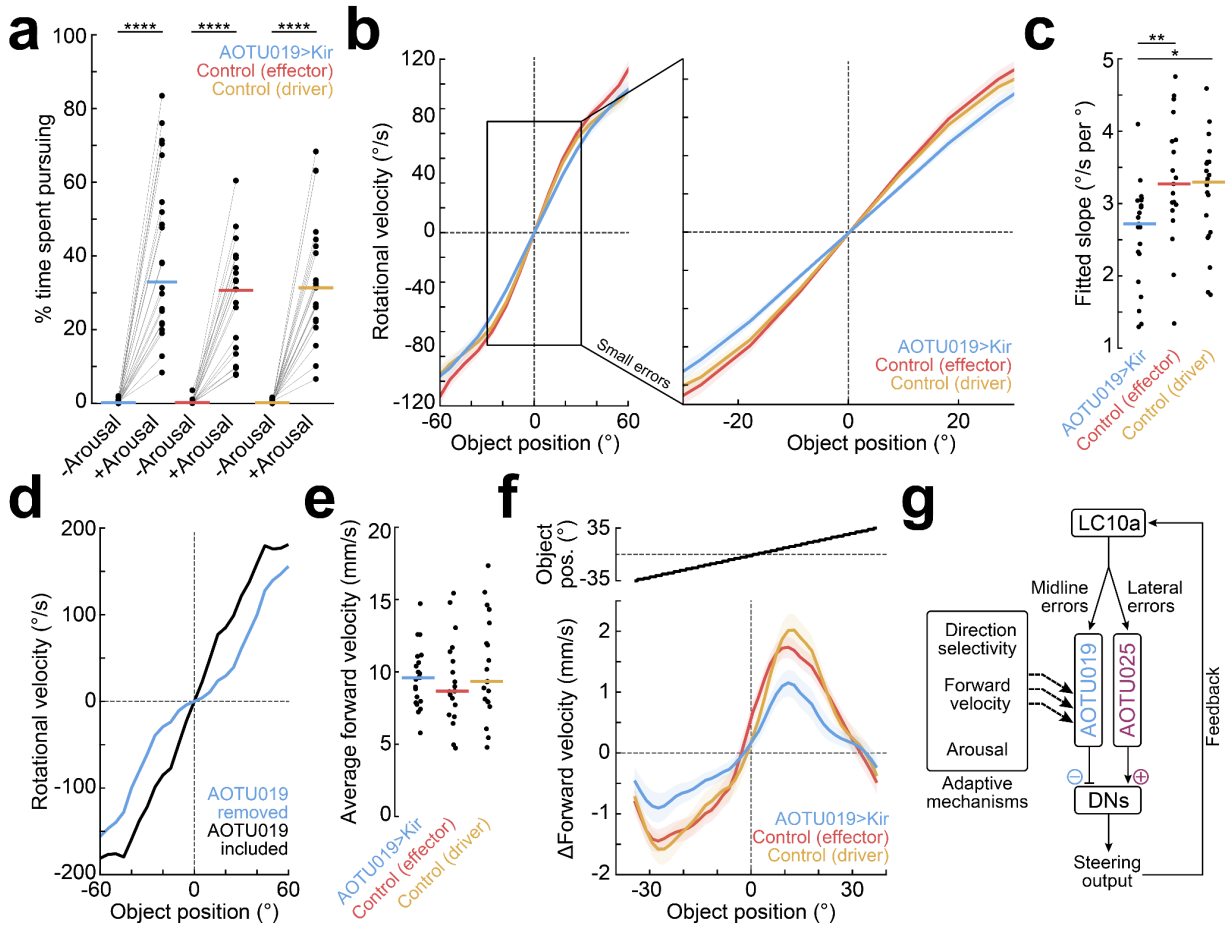


**Figure 6: Silencing the frontal pathway impairs object-directed steering during arousal.**

**a**, Percentage of time each male flies spent pursuing a fictive "female" following arousal stimulation for AOTU019>Kir (n = 21 flies), effector control (n = 19 flies), and driver control (n = 21 flies). P1 stimulation significantly increased pursuit behavior within each genotype ($p < 0.0001$, Bonferroni-corrected); genotype had no significant effect ($p = 0.99998$). Horizontal lines indicate medians.

**b**, Rotational velocity binned by virtual female position in the front field of view (<60°) during pursuit for AOTU019>Kir (n = 21 flies), effector control (n = 19 flies), and driver control (n = 21 flies) flies (mean ± s.e.m.). Magnified view of responses near the midline shows a consistent reduction in steering towards the female for AOTU019>Kir flies.

**c**, Slope distributions from the front field reveal a significant reduction in steering gain with AOTU019 silencing ($p < 0.05$, $p < 0.01$).

**d**, Simulation summary, for AOTU019 either included or removed, showing rotational velocity binned by object position. Minor LC10a-to-DNa02 visual-motor pathways included (**Fig. 1c, Fig. S7**). Removing AOTU019 reduces steering toward the object.

**f**, Distribution of average forward velocity during pursuit for AOTU019>Kir (n = 21 flies), effector control (n = 19 flies), and driver control (n = 21 flies) flies, revealing no significant difference across genotypes ($p = 0.477$).

**e**, Change in forward velocity binned by object position during open-loop pursuit of an oscillatory stimulus in AOTU019>Kir (n = 21), effector control (n = 19), and driver control (n = 21) flies (mean ± s.e.m.). Change measured from each fly's baseline speed. While the main effect of genotype was not significant ($p = 0.4331$), a significant interaction with object position ($p < 0.0001$) suggests that AOTU019 contributes to forward speed modulation near the visual midline.

**f**, Feedback control model of visual object pursuit in *Drosophila*, including adaptive control elements—enhanced direction selectivity, sensitivity to forward velocity, and arousal-dependent recruitment—implemented by the midline error correction pathway AOTU019.

## STAR Methods

## EXPERIMENTAL MODEL AND STUDY PARTICIPANT DETAILS

Flies expressing CsChrimson[88] were reared on cornmeal-molasses food (Archon Scientific) mixed with 100 µl all-*trans*-retinal (Sigma; 17 mM in ethanol) and wrapped in light-blocking foil to prevent photo-conversion. Flies not expressing CsChrimson were reared on standard cornmeal-molasses food. All flies were maintained in an incubator (Darwin Chambers) on a 12 h light:12 h dark cycle at 25 °C, 50-70% relative humidity. All experimental flies had at least one wild-type endogenous copy of the white (*w*) gene, represented by *w+* in the genotypes below. Genotypes were as follows:

**Fig. 1-5, S2, S5, S8-9:**
AOTU019 recording with P1 activation:
*w+ P{10XUAS-IVS-mCD8::GFP}su(Hw)attP8; P{R55E10-p65.AD}attP40/P{GMR71G01-lexA}attP40; P{VT033301-GAL4.DBD}attP2/PBac{13XLexAop2-IVS-CsChrimson.tdTomato}VK00005*
AOTU025 recording with P1 activation:
*w+ P{10XUAS-IVS-mCD8::GFP}su(Hw)attP8; P{VT041034-p65.AD}attP40/P{GMR71G01-lexA}attP40; P{R54A03-GAL4.DBD}attP2/PBac{13XLexAop2-IVS-CsChrimson.tdTomato}VK00005*

**Fig. 2, S4:**
DNa02 recording with P1 cell activation:
*w+; P{20XUAS-IVS-mCD8::GFP}attP40/P{GMR71G01-lexA}attP40; P{GMR87D07-GAL4}attP2/PBac{13XLexAop2-IVS-CsChrimson.tdTomato}VK00005*

**Fig. 2-4, S4:**
Behavioral measurements in intact flies with P1 activation:
*w+; P{VT034810-p65.AD}attP40/P{GMR71G01-lexA}attP40; P{VT033301-GAL4.DBD}attP2/PBac{13XLexAop2-IVS-CsChrimson.tdTomato}VK00005*
*w+; +/P{GMR71G01-lexA}attP40; +/P{pJFRC49-10xUAS-IVS-eGFP::Kir2.1}attP2 PBac{13XLexAop2-IVS-CsChrimson.tdTomato}VK00005*

**Fig. 5-6, S6:**
AOTU019 cells expressing Kir2.1 with P1 activation:
*w+; P{VT034810-p65.AD}attP40/P{GMR71G01-lexA}attP40; P{VT033301-GAL4.DBD}attP2/P{pJFRC49-10xUAS-IVS-eGFP::Kir2.1}attP2 PBac{13XLexAop2-IVS-CsChrimson.tdTomato}VK00005*
Effector control with P1 activation:
*w+; +/P{GMR71G01-lexA}attP40; +/P{pJFRC49-10xUAS-IVS-eGFP::Kir2.1}attP2 PBac{13XLexAop2-IVS-CsChrimson.tdTomato}VK00005*
Driver control with P1 activation:
*w+; P{VT034810-p65.AD}attP40/P{GMR71G01-lexA}attP40; P{VT033301-GAL4.DBD}attP2/PBac{13XLexAop2-IVS-CsChrimson.tdTomato}VK00005*

**Fig. S2:**
AOTU019 and Gad1 line:
*w+; P{20XUAS-IVS-mCD8::GFP}attP40/+; Mi{Trojan-p65AD.2}Gad1[MI09277-Tp65AD.2]/P{VT033301-GAL4.DBD}attP2*

**Fig. S6:**
AOTU019 cells expressing GFP and Kir2.1:
*w+; P{VT034810-p65.AD}attP40/P{20XUAS-IVS-mCD8::GFP}attP40; P{VT033301-GAL4.DBD}attP2/P{pJFRC49-10xUAS-IVS-eGFP::Kir2.1}attP2*
AOTU019 cells expressing GFP:
*w+; P{VT034810-p65.AD}attP40/P{20XUAS-IVS-mCD8::GFP}attP40; P{VT033301-GAL4.DBD}attP2/+*

**Origins of transgenic stocks**

The following stocks were obtained from the Bloomington Drosophila Stock Center (BDSC): split-Gal4 hemidrivers to target AOTU019 (BDSC_69919, BDSC_71336, BDSC_73717), split-GAL4 hemidrivers to target AOTU025 (BDSC_73987, BDSC_75635), *P{GMR87D07-GAL4}attP2* to target DNa02[51] (BDSC_48391), *P{GMR71G01-lexA}attP40* to target P1[47] (BDSC_54733), *PBac{13XLexAop2-IVS-CsChrimson.tdTomato}VK00005* (BDSC_82183), *P{20XUAS-IVS-mCD8::GFP}attP2* (BDSC_32194), split-Gal4 AD hemidriver expressed in Gad1+ neurons[50] (BDSC_60322). *P{pJFRC49-10xUAS-IVS-eGFP::Kir2.1}attP2* was a gift from G. Card, isogenized OregonR from T. Clandinin, and isogenized *P{10XUAS-IVS-mCD8::GFP}su(Hw)attP8* and *P{20XUAS-IVS-mCD8::GFP}attP40* from H. Yang. The recombined *P{pJFRC49-10xUAS-IVS-eGFP::Kir2.1}attP2 PBac{13XLexAop2-IVS-CsChrimson.tdTomato}VK00005* and AOTU019 split-Gal4 stocks backcrossed for five generations into the isoD1 background were generated in-house.

We validated the expression of the constructed AOTU019 and AOTU025 split-Gal4 lines using immunohistochemical anti-GFP staining and also by comparison against available Multi-Color-Flip-Out (MCFO) image libraries[89,90].

**METHOD DETAILS**

**Fly preparation and dissection**

Male flies were collected on $CO_2$ and had their wings clipped (to reduce grooming) the day before experiments, and were housed overnight at low density (≤8 flies per vial) in vials of cornmeal molasses food supplemented with all-*trans*-retinal. All experiments used male flies 16–30 h post-eclosion without circadian timing restrictions. To prepare an experiment, flies were briefly cold-anesthetized and fit into an inverted pyramid-shaped platform (black Delrin, Protolabs). This platform design minimized eye occlusion and maximized body and leg mobility. The fly's head and thorax were secured with UV-curable glue (Loctite AA 3972, Henkel), cured with UV light pulses (LED-200, Electro-Lite Co.). For behavioral experiments on intact flies, flies were secured into the platform, but no further dissection was performed. For electrophysiology experiments, after the fly was secured in the platform, the proboscis was immobilized by severing the lateral muscles and securing the appendage with UV-curable glue while the fly was cold-anesthetized (to reduce brain movement). After several minutes of recovery time, a small window was cut in the dorsal cuticle under oxygenated saline. Tracheoles, fat, and perineurial glia sheath were removed. Muscle 16 (and often the esophagus) was severed to further reduce brain movement. Prior to data collection, all flies were given a 20-minute acclimation period on the spherical treadmill with the visual cue rotating in closed loop with the fly's rotation.

**Experimental recording setups**

Electrophysiology experiments used a semi-custom upright microscope with a motorized base (Thorlabs), epifluorescence turret (BX51, Olympus), 40× water immersion objective (LUMPlanFLN 40×W, Olympus), and CCD Monochrome Camera (Retiga ELECTRO, Teledyne Photometrics). The substage optics were removed to fit the treadmill and visual panorama. The brain was back-illuminated with a far-red LED (M780L3, Thorlabs). For GFP or CsChrimson excitation, a 100 W Hg arc lamp (U-LH100HG, Olympus), controlled by an optical shutter, provided blue (480 nm) or red (620-660 nm) light through the objective, respectively. Red light was dimmed using neutral density filters (~4 μW/mm² at 600 nm). The microscope was enclosed in a Faraday cage and blackout material, and mounted on an air-supported table for vibration isolation.

Patch-clamp recordings were made using an Axopatch 200B amplifier (Molecular Devices), low-pass filtered at 5 kHz, and acquired at 20 kHz. Oxygenated saline (28-30 °C) superfused the brain during experiments. Saline contained (in mM): 103 NaCl, 3 KCl, 5 TES, 8 trehalose, 10 glucose, 26 $NaHCO_3$, 1 $NaH_2PO_4$, 1.5 $CaCl_2$, and 4 $MgCl_2$ (osmolarity adjusted to 270–273 mOsm, pH ~7.3). Remaining perineural sheath or cell bodies were cleared using saline-filled "cleaning pipettes" pulled from thin-wall capillaries (TW150F-3, World Precision Instruments). Cell recordings were made using patch pipettes (6-12 MΩ) pulled from filamented borosilicate glass (B150-86-7.5HP, Sutter Instrument) and filled with 0.22-μm filtered internal solution, containing (in mM): 140 potassium aspartate, 10 HEPES, 4 MgATP, 0.5 $Na_3GTP$, 1 EGTA, 1 KCl, and 13 biocytin hydrazide (pH 7.3, osmolarity adjusted to 268 mOsm). All data was acquired at 20 kHz (NiDAQ PCIe-6251, National Instruments).

**Spherical treadmill and locomotion measurement**

An air-cushioned spherical treadmill equipped with a machine vision system was used to track the animal's intended movements. The treadmill consisted of a 9 mm diameter foam ball (FR-4615, General Plastics) floated in a custom concave holder (ABS Black, Protolabs) using medical-grade breathing air (Med-Tech) regulated via an inline flow meter (Cole Parmer). For tracking, the ball was marked with a high-contrast pattern and illuminated by a far-red LED (M780L3, Thorlabs). A CMOS camera (GS3-U3-51S5M, Teledyne FLIR) with an adjustable zoom lens (M7528-MP, Computar) captured ball movement at 60 Hz. FicTrac v2.1[91] tracked ball position, with a custom Python script for transmitting forward, sideways, rotational, and gain-modified rotational displacements to an analogue output device (PhidgetAnalog 4-Output), acquired at 20 kHz (NiDAQ PCIe-6251, National Instruments). In some experiments (where specifically reported), the visual cue rotated in closed loop with the fly's rotation on the spherical treadmill.

**Visual panorama**

Visual stimuli were displayed using a circular panorama of modular 16×16 pixel LED panels[92], with each pixel subtending ~1.5° of the animal's visual field and covering 48° in height and 336° in azimuth. The rear column (24°) was removed for ball illumination and tracking equipment. Green LEDs (525 nm) were used for electrophysiology and blue LEDs (465 nm) for experiments focused exclusively on behavioral measurements. Diffuser film (SXF-0600, Decorative Films) and gel filters (RE131 and RE071, Rosco) reduced reflections and intensity. For electrophysiology experiments, the panorama was grounded with fine copper mesh. The panorama, controlled at 500 Hz using a reconfigurable I/O device (PCIe-7842R, National Instruments) and display tools from M. Reiser (https://reiserlab.github.io/Modular-LED-Display/G4/), provided real-time output of visual cue position and gain-modified displacement via a breakout box (CB-68LPR, National Instruments) to the data acquisition card.

For visual object pursuit, the visual stimulus was a dark vertical bar (10.5°) on a bright background. For optomotor response experiments, a full-field square wave grating with a 12° period was used. In experiments without a visual object, the panorama was uniformly illuminated at low intensity.

**Visual stimuli (open-loop and closed-loop)**

During some experiments, flies were presented with three stimuli that moved in three fixed patterns, irrespective of the fly's own movements ("open loop"): (1) an object appearing randomly every 3 s, sweeping 22.5° at 25°/s or 75°/s, then disappearing ("motion pulses"), with motion paths tiling the front 100° of the visual field (for AOTU019) or the front 180° of the visual field (for AOTU025 and for behavior experiments in intact flies), (2) an object moving back and forth across the visual field following a triangle wave pattern with an amplitude of ±35° at speeds of 15, 25, 35, 55, or 75°/s ("oscillating object"), and (3) full-field square-wave vertical gratings alternating clockwise/counterclockwise at 75°/s ("optomotor stimuli").

During experiments where the visual object rotated around the panorama in "closed loop", the object's azimuthal position was controlled by the spherical treadmill's rotational displacement: when the spherical treadmill rotated to the right (signaling an attempted left turn by the fly), the object also rotated right, and *vice versa*. Every 30 s, the visual object "jumped" 60° left or right relative to the object's current position, and at each time step, we also added random motion to the visual object; these perturbations challenged the male pursuit system to keep the object near the male's visual midline. The random motion was drawn from a standard normal distribution (mean = 0, SD = 1), low-pass filtered at 2 Hz (−3 dB corner frequency, Butterworth filter), then mean-subtracted and scaled to have a standard deviation of 3°.

In closed loop experiments, the ratio of object rotation to spherical treadmill rotation was varied from 0.95× to 2×, with a ratio chosen randomly on each trial from a set of fixed ratios. The 0.95× ratio was used to compare behavior before and after arousal stimulation in Figure 5. Varying the object ratio was intended to challenge the male's ability to correct his trajectory during pursuit, however, we found no significant effect of this ratio on the percentage of time the male spent pursuing the object ($p = 0.3588$), the estimated lag between the visual object's position and the male's rotational velocity ($p = 0.7396$), or the fitted slope of the function relating rotational velocity to object position ($p = 0.8594$). Thus, in Figures 4, 6, and S6, we pooled data across ratios per fly for analysis of closed loop experiments.

**Behavioral observations in intact flies**

For experiments where we tested the effect of Kir2.1 expression in AOTU019 neurons, along with the relevant driver control and effector control, the experimenter was blinded to genotype during data collection, and genotypes were interleaved randomly. Flies were secured into our standard fly-restraining platform (described above), but no further dissection was performed. The fly and the visual panorama were placed inside an enclosure warmed to 25-30°C with a fan heater. The enclosure was covered in blackout material to reduce visual disruptions and mounted on sorbothane feet (AV4, Thorlabs) to reduce vibrations. For CsChrimson excitation, a red LED (M660L4, Thorlabs) was positioned above the fly (~40 μW/mm² at 600 nm) and controlled by a LED driver (LEDD1B, Thorlabs). All data was acquired at 20 kHz (NiDAQ PCIe-6251, National Instruments).

**Experiment trial structure**

To motivate males to engage in pursuit, we optogenetically stimulated CsChrimson-expressing P1 cells with red light delivered for the full trial duration. For electrophysiology, experiments routinely began with

alternating light pulses (15 s off, 15 s on) to stimulate P1 cells and measure baseline membrane potential and firing rate without visual stimuli. For motion pulse experiments, different motion pulses were presented in pseudo-random order. For oscillating object experiments, different object speeds were presented in pseudo-random order. Trials without arousal stimulation, using a 35°/s object, were randomly interleaved between oscillating object trials. Between motion pulse and oscillating object trials, flies were given 5-10 s breaks without arousal stimulation.

To manipulate cell activity, brief current injections (1 s every 5 s) were delivered via the recording electrode to depolarize (+100 pA) or hyperpolarize (-75 pA) AOTU019, and depolarize (+20-40 pA) or hyperpolarize (-15-20 pA) AOTU025, as males walked without visual stimuli. Current magnitudes were selected to elicit comparable changes in firing rate across cell types. Generally, hyperpolarization largely or completely suppressed spiking, while depolarization increased firing rates by 30–50 spikes/s. Step order was randomly assigned per trial.

### Immunohistochemistry

Brains were dissected 1–2 days post-eclosion in external saline, fixed in 4% paraformaldehyde (Electron Microscopy Sciences) in PBS (Thermo Fisher Scientific) for 15 min at room temperature, and washed with PBS. After a 20-min block in 5% normal goat serum (Sigma-Aldrich) in PBS with 0.44% Triton-X (Sigma-Aldrich), samples were incubated ~24 h with primary antibodies in blocking solution, washed with PBS, and incubated ~24 h with secondary antibodies. Brains were rinsed, mounted in antifade medium (Vectashield, Vector Laboratories), and imaged on a Leica confocal microscope (SPE, SP8X, or Stellaris) with a 20× or 40× oil-immersion objective. Image stacks included 50–200 z-slices (1 μm depth, 1,024×1,024 pixels, 3 line averages). For Gal4 and lexA expression, primary antibodies were chicken anti-GFP (1:1,000, Abcam), rabbit anti-RFP (1:100, Abcam), and mouse anti-Bruchpilot (1:30, nc82, DSHB). Secondary antibodies included Alexa Fluor 488 anti-chicken, Alexa Fluor 568 anti-rabbit, and Alexa Fluor 633 anti-mouse (1:250, Invitrogen).

## QUANTIFICATION AND STATISTICAL ANALYSIS

### Data processing

For locomotion data, the forward, sideways, and rotational positions of the ball were computed in real time and acquired as voltage signals. Post hoc, these signals were converted to radians, unwrapped, low-pass filtered at 20 Hz, downsampled to 1,000 Hz, converted to degrees, and smoothed with a Gaussian window ($\sigma$ = 200 ms). Directional velocities ($\Delta$position/$\Delta$t) were calculated and smoothed with a Gaussian window ($\sigma$ = 100 ms). Rotational velocity was then converted to in °/s, and forward/sideways velocities to mm/s (based on the diameter of the spherical treadmill). Visual panorama data, acquired as voltage signals, were converted to degrees post-hoc.

For electrophysiology data, the liquid junction potential was corrected post hoc by subtracting 13 mV from recorded voltages[93]. Cell firing rate was estimated by detecting spikes in the membrane voltage signal (using the findpeaks function in MATLAB) and convolving the resulting binary spike train with either a Gaussian kernel ($\sigma$ = 50 ms, window = ±500 ms) or a causal exponential kernel ($\tau$ = 125 ms, window = 0–1.25 s), each scaled such that the total area under the kernel was unity. A Gaussian kernel was used for all analyses except for the current injection experiments, where a causal kernel was used to better resolve the temporal relationship between manipulated neural activity and behavioral output.

### Classification of behavioral epochs

Running epochs were classified using a Schmitt trigger on forward velocity: running epochs began when forward velocity exceeded 5 mm/s (for behavioral observations in intact flies) or 3 mm/s (for electrophysiology-and-behavior experiments), and running epochs ended when forward velocity fell below 0.1 mm/s. Running epochs shorter than 5 s were excluded. Stationary epochs were defined as all periods outside of running, including timepoints where forward velocity was within ±0.25 mm/s (to account for minor vibrations and movements of the fly on the ball).

During experiments where the visual cue rotated in closed loop with the fly's rotation, pursuit epochs were identified by first calculating the mean object position over a 2-s sliding window (1.5-ms steps) and then finding periods where the mean position remained within ±35° of the midline while the fly was running[94,95]. Epochs with short gaps in pursuit (<2 s) were included. Epochs of pursuit shorter than 5 s were excluded, as were the first/last 2 s of each trial.

During experiments where the visual object's movements were purely open-loop, the pursuit index[20] was calculated using a 5 s sliding window (50 ms steps) and defined as the product of tracking fidelity (correlation between visual object position and the fly's rotational velocity) and vigor (net ipsilateral turning normalized to 1). The first and last 5 s of each trial were excluded.

**Computing responses to open-loop visual stimuli**

To assess behavioral and neural responses to open-loop visual stimuli, each animal's average evoked response was calculated, segregated by relevant behavioral state (e.g., all, running only, or stationary only) during the visual stimulus presentation. Stimulus presentations were assigned to a behavioral state if >70% of the timepoints in the stimulus presentation met the criterion. To correct for an individual animal's turning biases (e.g., a tendency to turn more left or right due to innate preference and/or placement on the ball), turn responses to left and right stimuli were mirrored and averaged. Visual response latency was defined as the time from the start of the visual motion pulse to the first peak in the time-derivative of firing rate, measured during stationary epochs at each cell's preferred object position. For summary plots, each motion pulse was assigned to its center position (°): −123.75, −101.25, −78.75, −56.25, −33.75, −11.25, 11.25, 33.75, 56.25, 78.75, 101.25, 123.75, 146.25, where negative values represent positions in the left visual field. In some plots, to improve clarity, traces were slightly offset to the left or right of center along the x-axis to reduce overlap.

We computed the expected right–left (R–L) firing rate on a per-cell basis, from the perspective of a right-hemisphere cell, under the assumption that R and L cells have mirror-symmetric tuning properties. For example, during a rightward (ipsiversive) motion pulse presented on the right (ipsilateral) visual field, the R cell's response was taken as the measured firing rate. To estimate the corresponding response from a left-hemisphere cell to rightward pulses in the right visual field, we took this R cell's response to leftward (contraversive) motion on the left (contralateral) visual field. Using this procedure, we used each recorded R cell to generate an estimate of the the R-L response to each motion pulse as:

$$L_{rightward}(\theta) = R_{leftward}(-\theta)$$

$$R - L_{rightward}(\theta) = R_{rightward}(\theta) - L_{rightward}(\theta) \qquad \text{Eq. 1}$$

Here, θ is the angular position corresponding to the center of the motion pulse. We used the equivalent procedure to compute $R - L_{leftward}(\theta)$. We used error propagation to determine the error associated with R-L differences, where propagated error was calculated as the square root of the sum of squared standard errors from the individual components.

The direction selectivity index (DSI) was calculated by comparing firing rate (FR) responses to ipsiversive versus contraversive motion at the same visual stimulus position[20], expressed as the difference divided by the sum of the two responses per cell:

$$DSI = \frac{FR_{ipsiversive} - FR_{contraversive}}{FR_{ipsiversive} + FR_{contraversive}} \quad \text{Eq. 2}$$

where ipsiversive means rightward for a cell in the right hemisphere.

**Computing responses to closed-loop visual stimuli**

To standardize fixation angles across flies, visual object positions were centered at 0° by subtracting the mean visual object position during fixation. This procedure assumes that each fly is attempting to fix the object precisely at 0°, and so any small systematic biases in a fly's mean fixation angle are due to imprecision in setting the fly's azimuthal angle relative to the display screen, or other similar sources of measurement error. To analyze the relationship between visual object position and turning behavior during closed-loop fixation, average rotational velocity (adjusted for visuomotor delay) was computed in 9° visual object position bins for each fly. Linear regressions were fit for visual object positions between ±20° by genotype, with slopes, confidence intervals, and Pearson correlation coefficients calculated per fly.

**Computing the relationship between neural activity and behavior**

To examine relationships between neural activity and behavior, average firing rates were computed for each fly in bins of 1 mm/s for forward velocity, 20°/s for rotational velocity, and 0.05 for the pursuit index to assess neural activity and pursuit performance. Similarly, average rotational velocity was computed for each fly in bins of 5 spikes/s. To assess temporal relationships between neural activity and behavior, we computed the cross-correlation between firing rate and lagged changes in directional velocity over a ±1 s window in 1.5 ms steps. For rotational velocity analyses, only ipsilateral (same-side) turns relative to the recorded neuron were considered. Cells were excluded from analysis of lag times if their cross-correlation did not exhibit a clear peak, defined as a minimum prominence of 0.15, because the lag associated with the peak correlation is not interpretable if the peak correlation is particularly weak. Data within 140 ms of walking onset or 250 ms before walking offset were excluded, as were the first and last 250 ms of P1 stimulation trials.

For current injection experiments, the average evoked response was calculated per fly for depolarizing and hyperpolarizing injections (1 s) within a 3 s window. Analyses were restricted to current injection trials during which the animal was actively walking (forward velocity >3 mm/s for more than 30% of the analysis window). Change in forward and rotational velocity was quantified by subtracting the average velocity during the 500 ms baseline period preceding current onset from the average during the final 500 ms of the pulse.

**Statistical analyses**

Statistical analyses were performed in MATLAB. We used paired and two-sample Student's t-tests, as well as ANOVAs to assess main effects, with post hoc Tukey-Kramer tests for pairwise comparisons where appropriate. For all repeated-measures ANOVAs, fly identity was modeled as a random effect using a linear mixed-effects model to account for within-animal variability. The p-values for all statistical tests are in **Table S1**, and are reported in the figures as: $p < 0.05$ (*), $p < 0.01$ (**), $p < 0.001$ (***), and $p < 0.0001$ (****).

**Data exclusion, sample sizes, and data reporting**

Flies that displayed <20 s of pursuit were excluded. For electrophysiology experiments, trials continued until the fly stopped walking or recording quality degraded (10–120 min). For analyzing the relationship between changes in firing rate and behavior, flies that displayed <60 s of forward walking were excluded. For current injection experiments, we focused on cases where the injection effectively changed firing rate; thus, cells that showed firing rate changes of <10 spikes/s following depolarization or hyperpolarization were excluded, and individual current pulses that evoked firing rate changes in the bottom quartile (within each cell) were excluded. Sample sizes were based on field standards, informed by pilot experiments evaluating animal-to-animal variance and optimizing visual stimuli, rearing conditions, and stimulation intensities.

In all analyses combining data across flies, where we report mean, median, and/or s.e.m., these values were calculated across flies for all analyses, not across trials; before computing these descriptive statistics across flies, we took the average of each fly's responses on different presentations of the same stimulus. Thus, reported replicates (n values) represent the number of flies, not the number of stimulus presentations. A maximum of one neuron was recorded per fly.

**Analyzing connectome data**

Proofread cell reconstructions[38,39], synaptic connectivity data[38,40,84,85], and neurotransmitter type predictions[49] were taken from the FAFB (Female Adult Fly Brain) connectome[38,40] (v783, https://ngl.flywire.ai/) and analyzed using fafbseg[96] (v0.14.1, https://natverse.org/). Connections with <5 synapses were excluded from all analyses[41]. NeuronBridge[90] was used to identify potential driver lines for targeting AOTU019 and AOTU025.

Receptive fields of AOTU cells postsynaptic to LC10a were estimated by mapping the lobula's medial-lateral axis onto the anterior-posterior retinotopic axis[97]. LC10a meshes were assigned anterior-posterior coordinates (-15° to 165°)[86,87] based on their full distribution. Synaptic inputs were color-coded by weight, averaged along the lobula's medial-lateral axis, smoothed with a Gaussian filter, and mapped to the anterior-posterior coordinate frame. Dorsal lobula regions, primarily containing cell bodies and axonal projections, were excluded.

Neuron cable width was analyzed by skeletonizing neurons from the FAFB (Flywire v630) dataset using the "wave-front" skeletonization method[41]. Median primary dendrite widths were calculated for within-brain comparisons and visualized as normalized kernel density estimates. Measurements, based on dehydrated brain data, may underestimate true values.

**Network model**

The model was run in MATLAB 2024a at 100 Hz, iterating 20,000 times per condition. The LC10a receptive field estimates for each AOTU cell were computed from connectome data (**Fig. 1e**), and were used to generate a lookup table of predicted neural activity as a function of the time-varying object position ($\theta(t)$) in azimuthal space. Left and right copies of each AOTU cell were assumed to have mirror-symmetric visual receptive fields. The contribution of each AOTU cell was then weighted according to the number of synapses it forms onto DNa02 (averaged across hemispheres). Left and right copies of each AOTU cell were assigned identical output weights onto their ipsilateral copy of DNa02. We then modeled the activity of each DNa02 over time by linearly combining its AOTU inputs. Because AOTU019 is inhibitory and projects to the contralateral copy of DNa02, its contribution was sign-inverted and left-right inverted:

$$\begin{aligned} DNa02R(\theta(t)) &= AOTU025R(\theta(t)) - AOTU019L(\theta(t)) \\ DNa02L(\theta(t)) &= AOTU025L(\theta(t)) - AOTU019R(\theta(t)) \end{aligned} \qquad \text{Eq. 3}$$

The fly's rotational velocity command $r(\theta(t))$ was taken as proportional to the right-left difference in DNa02 activity[35]:

$$r(\theta(t)) \;=\; k(DNa02R(\theta(t)) \;-\; DNa02L(\theta(t))) \qquad \text{Eq. 4}$$

In this model, $r$>0 indicates rightward (clockwise) steering. The scalar parameter $k$ defines the size of the rotational velocity response resulting from a given R-L difference in DNa02 activity. Rotational velocity was used to update the fly's azimuthal orientation after a delay (Δt) of 200 ms, i.e. 20 steps of simulated time, to emulate the measured delay between neural activity and the rotation of the spherical treadmill. Rightward rotational velocity causes a negative (leftward) change in the object's position $\theta(t)$, and vice versa. Thus, the object position evolves over time in response to the fly's steering commands:

$$\theta(t) \;=\; \theta(t-1) \;-\; r(\theta(t-\Delta t)) \;+\; (\xi(t)\cdot\alpha) \qquad \text{Eq. 5}$$

where $\xi(t)$ is a random component scaled by a fixed scalar α. For each run, $\xi(t)$ was sampled from a normal distribution using the same frozen noise sample and then low-pass filtered at 2 Hz to generate a slowly-varying random perturbation of the object, emulating female movements during courtship. To quantify the model's ability to steer the object toward the midline and maintain this setpoint despite this perturbation, we calculated the probability of the object remaining within ±10° of the midline (0°). Additionally, to measure the relationship between visual object position and the steering output of the model, we calculated the average rotational velocity (accounting for visuomotor delay) in 2° bins.

We also tested the model's ability to correct a step displacement of the object. To eliminate the effect of the delay in the model, we held the object displaced at the fixed position (e.g., 100°) for 1 s before allowing a corrective response. In this simulation, $\xi(t)$ was sampled from the same normal distribution as before, but the scale of the random component (α) was decreased 10-fold, to better illustrate the model dynamics resulting from overshooting. To quantify the model's ability to restore a stable setpoint following a large perturbation, we calculated the settling time, defined as the time required for the object position in each run to stabilize within a ±2° tolerance and remain within this range for >1 s.

Subsequently, in another model variant, we added direction selectivity to the AOTU019 pathway. The AOTU019 direction selectivity index (DSI) was set to 0.7 (based on electrophysiological measurements from AOTU019) to reduce the responses of the right-hemisphere cell to leftward object motion, and vice versa. In a separate analysis, the same manipulation was applied to the AOTU025 pathway instead.

In the last model variant, we eliminated AOTU019 in order to replicate a similar manipulation to our genetic silencing experiment. Here we included all AOTU cells postsynaptic to LC10a and presynaptic to DNa02, taking each cell's visual receptive field estimate from its LC10a inputs in the connectome (**Fig. S7**), and scaling each cell's response by its output weight onto DNa02. As all inputs are predicted to be excitatory[49], their contributions were weighted by the number of synapses they form onto DNa02 and summed to produce a combined AOTU drive to DNa02 from each hemisphere. For the right side:

$$AOTU_R(\theta(t)) = AOTU025R(\theta(t)) + AOTU027R(\theta(t)) + CB2070R(\theta(t)) + CB2070R(\theta(t)) + CB0007R(\theta(t)) + CB0007R_2(\theta(t)) + CB0007R(\theta(t)) + AOTU015aR(\theta(t)) + AOTU015aR(\theta(t)) + AOTU026R(\theta(t)) + AOTU015bR(\theta(t)) + LAL027R(\theta(t)) + CB0359R(\theta(t)) \qquad \text{Eq. 6}$$

and equivalently for the left side. Some neuron types (e.g., CB2070, AOTU015a) appear multiple times to reflect the presence of multiple cells of the same type, however, each cell's receptive field was modeled independently.

**KEY RESOURCES TABLE**

| REAGENT or RESOURCE | SOURCE | IDENTIFIER |
|---|---|---|
| **Antibodies** | | |
| Alexa Fluor 488 goat anti-chicken | Invitrogen | A11039 |
| Alexa Fluor 568 goat anti-rabbit | Invitrogen | A11011 |
| Alexa Fluor 633 goat anti-mouse | Invitrogen | A21050 |
| chicken anti-GFP | Abcam | ab13970 |
| rabbit anti-RFP | Abcam | ab62341 |
| mouse anti-Bruchpilot (nc82) | DSHB | nc82-s |
| **Chemicals, peptides, and recombinant proteins** | | |
| all-trans retinal | Sigma-Aldrich | CAS: 116-31-4 |
| **Experimental models: Organisms/strains** | | |
| *D. melanogaster*: isoD1 strain | Gift from T. Clandinin and H. Yang | N/A |
| *D. melanogaster:* Mi{Trojan-p65AD.2}Gad1[MI09277-Tp65AD.2] | Bloomington Drosophila Stock Center | RRID: BDSC_60322 |
| *D. melanogaster:* PBac{y[+mDint2] w[+mC]=13XLexAop2-IVS-CsChrimson.tdTomato}VK00005 | Bloomington Drosophila Stock Center | RRID: BDSC_82183 |
| *D. melanogaster:* P{pJFRC49-10xUAS-IVS-eGFP::Kir2.1}attP2 | Gift from G. Card | N/A |
| *D. melanogaster:* P{pJFRC49-10xUAS-IVS-eGFP::Kir2.1}attP2, PBac{y[+mDint2] w[+mC]=13XLexAop2-IVS-CsChrimson.tdTomato}VK00005 | This study (two pre-existing transgenes recombined on the same chromosome) | N/A |
| *D. melanogaster:* P{y[+t7.7] w[+mC]=GMR71G01-lexA}attP40 | Bloomington Drosophila Stock Center | RRID: BDSC_54733 |
| *D. melanogaster:* P{y[+t7.7] w[+mC]=GMR87D07-GAL4}attP2 | Bloomington Drosophila Stock Center | RRID: BDSC_48391 |
| *D. melanogaster:* P{y[+t7.7] w[+mC]=R54A03-GAL4.DBD}attP2 | Bloomington Drosophila Stock Center | RRID: BDSC_75635 |
| *D. melanogaster:* P{y[+t7.7] w[+mC]=R55E10-p65.AD}attP40 | This study (backcrossed into isoD1 background) | RRID: BDSC_69919 |
| *D. melanogaster:* P{y[+t7.7] w[+mC]=VT033301-GAL4.DBD}attP2 | This study (backcrossed into isoD1 background) | RRID: BDSC_73717 |
| *D. melanogaster:* P{y[+t7.7] w[+mC]=VT034810-p65.AD}attP40 | This study (backcrossed into isoD1 background) | RRID: BDSC_71336 |
| *D. melanogaster:* P{y[+t7.7] w[+mC]=VT041034-p65.AD}attP40 | Bloomington Drosophila Stock Center | RRID: BDSC_73987 |
| *D. melanogaster:* P{y[+t7.7] w[+mC]=10XUAS-IVS-mCD8::GFP}su(Hw)attP8 | Gift from H. Yang (backcrossed into isoD1 background) | RRID: BDSC_32189 |
| *D. melanogaster:* P{y[+t7.7] w[+mC]=20XUAS-IVS-mCD8::GFP}attP2 | Bloomington Drosophila Stock Center | RRID: BDSC_32194 |

| | | |
|---|---|---|
| *D. melanogaster:* P{y[+t7.7] w[+mC]=20XUAS-IVS-mCD8::GFP}attP40 | Gift from H. Yang (backcrossed into isoD1 background) | N/A |
| **Software and algorithms** | | |
| FicTrac (v2.1) | Moore et al.[91] | rjdmoore.net/fictrac |
| visual panorama display tools | Isaacson et al.[92] | https://reiserlab.github.io/Modular-LED-Display/G4/ |
| SpinView (v2.3.0.77) | FLIR Systems, Inc. | www.flir.com/products/spinnaker-sdk |
| natverse | Bates et al.[96] | natverse.org |
| MATLAB (2023b, 2024a) | MathWorks | RRID: SCR_001622 |
| Micro-Manager (v2.0.0) | Edelstein et al.[98] | RRID: SCR_000415 |
| R (v4.4.2) | R Project for Statistical Computing | RRID: SCR_001905 |
| R Studio (v2024.12.0) | Posit | RRID: SCR_000432 |
| **Other** | | |
| cornmeal-molasses food | Archon Scientific | recipe B2 |
| diffuser film | Decorative Films | SXF-0600 |
| filamented borosilicate glass | Sutter Instruments | B150-86-7.5HP |
| filter cube Cy5 Longpass | Chroma Technology | 49019 |
| filter cube ET-FITC/EGFP | Olympus America Inc. | OCT-49012BX2 |
| fly platform (inverted pyramid-shaped) | Protolabs | github.com/wilson-lab/design-files |
| gel filter, marine blue | Rosco | RE131 |
| gel filter, tokyo blue | Rosco | RE071 |
| mounted far-red LED | Thorlabs | M780L3 |
| mounted red LED | Thorlabs | M660L4 |
| thin-wall capillaries | World Precision Instruments | TW150F-3 |
| treadmill ball foam | General Plastics | FR-4615 |
| treadmill ball holder | Protolabs | github.com/wilson-lab/design-files |
| treadmill camera | Teledyne FLIR | GS3-U3-51S5M |
| UV-cured glue | Henkel Adhesives | Loctite AA 3972 |
| UV gun | Electro-Lite Co. | LED 200 |
| visual panorama | Isaacson et al.[92] | https://reiserlab.github.io/Modular-LED-Display/G4/ |

## References


1. Shadmehr, R., and Mussa-Ivaldi, S. (2012). Biological learning and control (MIT Press).
2. Barnes, G.R. (2008). Cognitive processes involved in smooth pursuit eye movements. Brain and Cognition *68*, 309–326.
3. Becker, W., and Fuchs, A.F. (1985). Prediction in the oculomotor system: smooth pursuit during transient disappearance of a visual target. Exp. Brain Res. *57*, 562–575.
4. Luebke, A.E., and Robinson, D.A. (1988). Transition dynamics between pursuit and fixation suggest different systems. Vision Res. *28*, 941–946.
5. Schwartz, J.D., and Lisberger, S.G. (1994). Initial tracking conditions modulate the gain of visuo-motor transmission for smooth pursuit eye movements in monkeys. Vis. Neurosci. *11*, 411–424.
6. Churchland, A.K., and Lisberger, S.G. (2002). Gain control in human smooth-pursuit eye movements. J. Neurophysiol. *87*, 2936–2945.
7. Garbutt, S., and Lisberger, S.G. (2006). Directional cuing of target choice in human smooth pursuit eye movements. J. Neurosci. *26*, 12479–12486.
8. Lisberger, S.G. (2015). Visual guidance of smooth pursuit eye movements. Annu. Rev. Vis. Sci. *1*, 447–468.
9. Kowler, E., Rubinstein, J.F., Santos, E.M., and Wang, J. (2019). Predictive smooth pursuit eye movements. Annu. Rev. Vis. Sci. *5*, 223–246.
10. Lancer, B.H., Evans, B.J.E., Fabian, J.M., O'Carroll, D.C., and Wiederman, S.D. (2022). Preattentive facilitation of target trajectories in a dragonfly visual neuron. Commun. Biol. *5*, 829.
11. Lohmann, A.C., Corcoran, A.J., and Hedrick, T.L. (2019). Dragonflies use underdamped pursuit to chase conspecifics. J. Exp. Biol. *222*, jeb190884.
12. Olberg, R.M., Worthington, A.H., and Venator, K.R. (2000). Prey pursuit and interception in dragonflies. J. Comp. Physiol. A *186*, 155–162.
13. Land, M.F., and Collett, T.S. (1974). Chasing behaviour of houseflies (Fannia canicularis): A description and analysis. J. Comp. Physiol. A Neuroethol. Sens. Neural Behav. Physiol. *89*, 331–357.
14. Geiger, G. (1981). Is there a motion-independent position computation of an object in the visual system of the housefly? Biol. Cybern. *40*, 71–75.
15. Bastock, M., and Manning, A. (1955). The Courtship of Drosophila Melanogaster. Behaviour *8*, 85–110.
16. Spieth, H.T. (1974). Courtship behavior in Drosophila. Annu. Rev. Entomol. *19*, 385–405.
17. Cook, R. (1979). The courtship tracking of Drosophila melanogaster. Biol. Cybern. *34*, 91–106.
18. Cook, R. (1980). The extent of visual control in the courtship tracking of D. melanogaster. Biol. Cybernetics *37*, 41–51.
19. Ribeiro, I.M.A., Drews, M., Bahl, A., Machacek, C., Borst, A., and Dickson, B.J. (2018). Visual projection neurons mediating directed courtship in Drosophila. Cell *174*, 607–621.e18.
20. Hindmarsh Sten, T., Li, R., Otopalik, A., and Ruta, V. (2021). Sexual arousal gates visual processing during Drosophila courtship. Nature *595*, 549–553.
21. Agrawal, S., Safarik, S., and Dickinson, M. (2014). The relative roles of vision and chemosensation in mate recognition of Drosophila melanogaster. J. Exp. Biol. *217*, 2796–2805.
22. Agrawal, S., and Dickinson, M.H. (2019). The effects of target contrast on courtship. J Exp Biol *222*. https://doi.org/10.1242/jeb.203414.
23. Sten, T.H., Li, R., Hollunder, F., Eleazer, S., and Ruta, V. (2023). Male-male interactions shape mate selection in Drosophila. bioRxiv. https://doi.org/10.1101/2023.11.03.565582.
24. Baxter, C., Mentlik, J., Shams, I., and Dukas, R. (2018). Mating success in fruit flies: courtship interference versus female choice. Anim. Behav. *138*, 101–108.
25. Dukas, R. (2020). Natural history of social and sexual behavior in fruit flies. Sci. Rep. *10*, 21932.
26. Wu, M., Nern, A., Williamson, W.R., Morimoto, M.M., Reiser, M.B., Card, G.M., and Rubin, G.M. (2016). Visual projection neurons in the Drosophila lobula link feature detection to distinct behavioral programs. Elife *5*. https://doi.org/10.7554/eLife.21022.
27. Otsuna, H., and Ito, K. (2006). Systematic analysis of the visual projection neurons of Drosophila melanogaster. I. Lobula-specific pathways. J. Comp. Neurol. *497*, 928–958.
28. Schretter, C.E., Hindmarsh Sten, T., Klapoetke, N., Shao, M., Nern, A., Dreher, M., Bushey, D., Robie, A.A., Taylor, A.L., Branson, K., et al. (2024). Social state alters vision using three circuit mechanisms in Drosophila. Nature, 1–8.
29. Schretter, C.E., Aso, Y., Robie, A.A., Dreher, M., Dolan, M.-J., Chen, N., Ito, M., Yang, T., Parekh, R., Branson, K.M., et al. (2020). Cell types and neuronal circuitry underlying female aggression in Drosophila. Elife *9*. https://doi.org/10.7554/eLife.58942.
30. Cheong, H.S.J., Eichler, K., Stürner, T., Asinof, S.K., Champion, A.S., Marin, E.C., Oram, T.B., Sumathipala, M., Venkatasubramanian, L., Namiki, S., et al. (2024). Transforming descending input into behavior: The organization of premotor circuits in the Drosophila Male Adult Nerve Cord connectome. eLife. https://doi.org/10.7554/elife.96084.1.
31. Marin, E.C., Morris, B.J., Stürner, T., Champion, A.S., Krzeminski, D., Badalamente, G., Gkantia, M., Dunne, C.R., Eichler, K.,

Takemura, S.-Y., et al. (2024). Systematic annotation of a complete adult male Drosophila nerve cord connectome reveals principles of functional organisation. eLife. https://doi.org/0.7554/eLife.97766.1.
32. Takemura, S.-Y., Hayworth, K.J., Huang, G.B., Januszewski, M., Lu, Z., Marin, E.C., Preibisch, S., Xu, C.S., Bogovic, J., Champion, A.S., et al. (2023). A connectome of the male *Drosophila* ventral nerve cord. eLife. https://doi.org/10.1101/2023.06.05.543757.
33. Phelps, J.S., Hildebrand, D.G.C., Graham, B.J., Kuan, A.T., Thomas, L.A., Nguyen, T.M., Buhmann, J., Azevedo, A.W., Sustar, A., Agrawal, S., et al. (2021). Reconstruction of motor control circuits in adult Drosophila using automated transmission electron microscopy. Cell *184*, 759–774.e18.
34. Chen, C.-L., Hermans, L., Viswanathan, M.C., Fortun, D., Aymanns, F., Unser, M., Cammarato, A., Dickinson, M.H., and Ramdya, P. (2018). Imaging neural activity in the ventral nerve cord of behaving adult Drosophila. Nat. Commun. *9*, 4390.
35. Rayshubskiy, A., Holtz, S.L., Bates, A., Vanderbeck, Q.X., Capdevila, L.S., and Wilson, R.I. (2024). Neural circuit mechanisms for steering control in walking Drosophila. eLife. https://doi.org/10.7554/elife.102230.1.
36. Feng, K., Khan, M., Minegishi, R., Müller, A., Van De Poll, M.N., van Swinderen, B., and Dickson, B.J. (2024). A central steering circuit in Drosophila. bioRxiv, 2024.06.27.601106. https://doi.org/10.1101/2024.06.27.601106.
37. Braun, J., Hurtak, F., Wang-Chen, S., and Ramdya, P. (2024). Descending networks transform command signals into population motor control. Nature *630*, 686–694.
38. Dorkenwald, S., Matsliah, A., Sterling, A.R., Schlegel, P., Yu, S.-C., McKellar, C.E., Lin, A., Costa, M., Eichler, K., Yin, Y., et al. (2024). Neuronal wiring diagram of an adult brain. Nature *634*, 124–138.
39. Schlegel, P., Yin, Y., Bates, A.S., Dorkenwald, S., Eichler, K., Brooks, P., Han, D.S., Gkantia, M., dos Santos, M., Munnelly, E.J., et al. (2024). Whole-brain annotation and multi-connectome cell typing of Drosophila. Nature *634*, 139–152.
40. Zheng, Z., Lauritzen, J.S., Perlman, E., Robinson, C.G., Nichols, M., Milkie, D., Torrens, O., Price, J., Fisher, C.B., Sharifi, N., et al. (2018). A Complete Electron Microscopy Volume of the Brain of Adult Drosophila melanogaster. Cell *174*. https://doi.org/10.1016/j.cell.2018.06.019.
41. Scheffer, L.K., Xu, C.S., Januszewski, M., Lu, Z., Takemura, S.-Y., Hayworth, K.J., Huang, G.B., Shinomiya, K., Maitlin-Shepard, J., Berg, S., et al. (2020). A connectome and analysis of the adult central brain. Elife *9*. https://doi.org/10.7554/eLife.57443.
42. Yang, H.H., Brezovec, B.E., Serratosa Capdevila, L., Vanderbeck, Q.X., Adachi, A., Mann, R.S., and Wilson, R.I. (2024). Fine-grained descending control of steering in walking Drosophila. Cell *187*, 6290–6308.e27.
43. Kimura, K.-I., Hachiya, T., Koganezawa, M., Tazawa, T., and Yamamoto, D. (2008). Fruitless and doublesex coordinate to generate male-specific neurons that can initiate courtship. Neuron *59*, 759–769.
44. von Philipsborn, A.C., Liu, T., Yu, J.Y., Masser, C., Bidaye, S.S., and Dickson, B.J. (2011). Neuronal control of Drosophila courtship song. Neuron *69*, 509–522.
45. Yamamoto, D., and Koganezawa, M. (2013). Genes and circuits of courtship behaviour in Drosophila males. Nat. Rev. Neurosci. *14*, 681–692.
46. Yu, J.Y., Kanai, M.I., Demir, E., Jefferis, G.S.X.E., and Dickson, B.J. (2010). Cellular organization of the neural circuit that drives Drosophila courtship behavior. Curr. Biol. *20*, 1602–1614.
47. Pan, Y., Meissner, G.W., and Baker, B.S. (2012). Joint control of Drosophila male courtship behavior by motion cues and activation of male-specific P1 neurons. Proc. Natl. Acad. Sci. U. S. A. *109*, 10065–10070.
48. Kohatsu, S., and Yamamoto, D. (2015). Visually induced initiation of Drosophila innate courtship-like following pursuit is mediated by central excitatory state. Nat. Commun. *6*, 6457.
49. Eckstein, N., Bates, A.S., Champion, A., Du, M., Yin, Y., Schlegel, P., Lu, A.K.-Y., Rymer, T., Finley-May, S., Paterson, T., et al. (2024). Neurotransmitter classification from electron microscopy images at synaptic sites in Drosophila melanogaster. Cell *187*, 2574–2594.e23.
50. Lacin, H., Chen, H.-M., Long, X., Singer, R.H., Lee, T., and Truman, J.W. (2019). Neurotransmitter identity is acquired in a lineage-restricted manner in the Drosophila CNS. eLife. https://doi.org/10.7554/eLife.43701.
51. Namiki, S., Dickinson, M.H., Wong, A.M., Korff, W., and Card, G.M. (2018). The functional organization of descending sensory-motor pathways in Drosophila. eLife. https://doi.org/10.7554/eLife.34272.
52. Schnell, B., Ros, I.G., and Dickinson, M.H. (2017). A descending neuron correlated with the rapid steering maneuvers of flying Drosophila. Curr. Biol. *27*, 1200–1205.
53. Summers, M.T., and Feller, M.B. (2022). Distinct inhibitory pathways control velocity and directional tuning in the mouse retina. Curr. Biol. *32*, 2130–2143.e3.
54. Grzywacz, N.M., and Amthor, F.R. (2007). Robust directional computation in on-off directionally selective ganglion cells of rabbit retina. Vis. Neurosci. *24*, 647–661.
55. Johnson, K.P., Fitzpatrick, M.J., Zhao, L., Wang, B., McCracken, S., Williams, P.R., and Kerschensteiner, D. (2021). Cell-type-specific binocular vision guides predation in mice. Neuron *109*, 1527–1539.e4.
56. Krauzlis, R.J., and Lisberger, S.G. (1994). A model of visually-guided smooth pursuit eye movements based on behavioral observations. J. Comput. Neurosci. *1*, 265–283.
57. Lisberger, S.G. (2010). Visual guidance of smooth-pursuit eye movements: sensation, action, and what happens in between. Neuron

*66*, 477–491.
58. Varennes, L., Krapp, H.G., and Viollet, S. (2020). Two pursuit strategies for a single sensorimotor control task in blowfly. Sci. Rep. *10*, 20762.
59. Wehrhahn, C., Poggio, T., and Bülthoff, H. (1982). Tracking and chasing in houseflies (Musca): An analysis of 3-D flight trajectories. Biol. Cybern. *45*, 123–130.
60. Reichardt, W., and Wenking, H. (1969). Optical detection and fixation of objects by fixed flying flies. Sci. Nat. *56*, 424–425.
61. Reichardt, W., and Poggio, T. (1976). Visual control of orientation behaviour in the fly. Part I. A quantitative analysis. Q. Rev. Biophys. *9*, 311–375, 428–438.
62. Reiser, M.B., and Dickinson, M.H. (2008). A modular display system for insect behavioral neuroscience. J. Neurosci. Methods *167*, 127–139.
63. Bahl, A., Ammer, G., Schilling, T., and Borst, A. (2013). Object tracking in motion-blind flies. Nat. Neurosci. *16*, 730–738.
64. Fenk, L.M., Poehlmann, A., and Straw, A.D. (2014). Asymmetric processing of visual motion for simultaneous object and background responses. Curr. Biol. *24*, 2913–2919.
65. Werblin, F.S. (2010). Six different roles for crossover inhibition in the retina: correcting the nonlinearities of synaptic transmission. Vis. Neurosci. *27*, 1–8.
66. Collett, T.S., and Land, M.F. (1975). Visual control of flight behaviour in the hoverfly Syritta pipiens L. J. Comp. Physiol. A Neuroethol. Sens. Neural Behav. Physiol. *99*, 1–66.
67. Collett, T.S., and Land, M.F. (1978). How hoverflies compute interception courses. J. Comp. Physiol. A Neuroethol. Sens. Neural Behav. Physiol. *125*, 191–204.
68. Olberg, R.M. (1986). Identified target-selective visual interneurons descending from the dragonfly brain. J. Comp. Physiol. A Neuroethol. Sens. Neural Behav. Physiol. *159*, 827–840.
69. Åström, K.J., and Murray, R.M. (2021). Feedback systems: An introduction for scientists and engineers, second edition (Princeton University Press).
70. Bidaye, S.S., Machacek, C., Wu, Y., and Dickson, B.J. (2014). Neuronal control of Drosophila walking direction. Science *344*, 97–101.
71. Jung, Y., Kennedy, A., Chiu, H., Mohammad, F., Claridge-Chang, A., and Anderson, D.J. (2020). Neurons that function within an integrator to promote a persistent behavioral state in Drosophila. Neuron *105*, 322–333.e5.
72. Deutsch, D., Pacheco, D., Encarnacion-Rivera, L., Pereira, T., Fathy, R., Clemens, J., Girardin, C., Calhoun, A., Ireland, E., Burke, A., et al. (2020). The neural basis for a persistent internal state in Drosophila females. Elife *9*. https://doi.org/10.7554/elife.59502.
73. Dowell, C.K., Lau, J.Y.N., Antinucci, P., and Bianco, I.H. (2024). Kinematically distinct saccades are used in a context-dependent manner by larval zebrafish. Curr. Biol. *34*, 4382–4396.e5.
74. Dowell, C.K., Hawkins, T., and Bianco, I.H. (2024). Subsets of extraocular motoneurons produce kinematically distinct saccades during hunting and exploration. bioRxiv, 2024.08.12.607184. https://doi.org/10.1101/2024.08.12.607184.
75. von Reyn, C.R., Breads, P., Peek, M.Y., Zheng, G.Z., Williamson, W.R., Yee, A.L., Leonardo, A., and Card, G.M. (2014). A spike-timing mechanism for action selection. Nat. Neurosci. *17*, 962–970.
76. Bidaye, S.S., Laturney, M., Chang, A.K., Liu, Y., Bockemühl, T., Büschges, A., and Scott, K. (2020). Two brain pathways initiate distinct forward walking programs in Drosophila. Neuron *108*, 469–485.e8.
77. Aymanns, F., Chen, C.-L., and Ramdya, P. (2022). Descending neuron population dynamics during odor-evoked and spontaneous limb-dependent behaviors. Elife *11*. https://doi.org/10.7554/eLife.81527.
78. Sapkal, N., Mancini, N., Kumar, D.S., Spiller, N., Murakami, K., Vitelli, G., Bargeron, B., Maier, K., Eichler, K., Jefferis, G.S.X.E., et al. (2024). Neural circuit mechanisms underlying context-specific halting in Drosophila. Nature *634*, 191–200.
79. Ros, I.G., Omoto, J.J., and Dickinson, M.H. (2024). Descending control and regulation of spontaneous flight turns in Drosophila. Curr. Biol. *34*, 531–540.e5.
80. Gonzalez-Bellido, P.T., Peng, H., Yang, J., Georgopoulos, A.P., and Olberg, R.M. (2013). Eight pairs of descending visual neurons in the dragonfly give wing motor centers accurate population vector of prey direction. Proc. Natl. Acad. Sci. U. S. A. *110*, 696–701.
81. Lin, H.-T., Siwanowicz, I., and Leonardo, A. (2024). Wireless recordings from dragonfly target detecting neurons during prey interception flight. bioRxiv, 2024.11.12.622977. https://doi.org/10.1101/2024.11.12.622977.
82. Westeinde, E.A., Kellogg, E., Dawson, P.M., Lu, J., Hamburg, L., Midler, B., Druckmann, S., and Wilson, R.I. (2024). Transforming a head direction signal into a goal-oriented steering command. Nature *626*, 819–826.
83. Mussells Pires, P., Zhang, L., Parache, V., Abbott, L.F., and Maimon, G. (2024). Converting an allocentric goal into an egocentric steering signal. Nature *626*, 808–818.
84. Buhmann, J., Sheridan, A., Malin-Mayor, C., Schlegel, P., Gerhard, S., Kazimiers, T., Krause, R., Nguyen, T.M., Heinrich, L., Lee, W.-C.A., et al. (2021). Automatic detection of synaptic partners in a whole-brain Drosophila electron microscopy data set. Nat. Methods *18*, 771–774.
85. Heinrich, L., Funke, J., Pape, C., Nunez-Iglesias, J., and Saalfeld, S. (2018). Synaptic cleft segmentation in non-isotropic volume electron microscopy of the complete Drosophila brain. In Medical Image Computing and Computer Assisted Intervention – MICCAI 2018 Lecture notes in computer science. (Springer International Publishing), pp. 317–325.

86. Heisenberg, M., and Wolf, R. (1984). Vision in Drosophila: Genetics of Microbehavior (Springer).
87. Shinomiya, K., Horne, J.A., McLin, S., Wiederman, M., Nern, A., Plaza, S.M., and Meinertzhagen, I.A. (2019). The Organization of the Second Optic Chiasm of the Drosophila Optic Lobe. Front. Neural Circuits *13*. https://doi.org/10.3389/fncir.2019.00065.
88. Klapoetke, N.C., Murata, Y., Kim, S.S., Pulver, S.R., Birdsey-Benson, A., Cho, Y.K., Morimoto, T.K., Chuong, A.S., Carpenter, E.J., Tian, Z., et al. (2014). Independent optical excitation of distinct neural populations. Nat Methods *11*, 338–346.
89. Meissner, G.W., Nern, A., Dorman, Z., DePasquale, G.M., Forster, K., Gibney, T., Hausenfluck, J.H., He, Y., Iyer, N.A., Jeter, J., et al. (2023). A searchable image resource of Drosophila GAL4 driver expression patterns with single neuron resolution. Elife *12*. https://doi.org/10.7554/eLife.80660.
90. Clements, J., Goina, C., Hubbard, P.M., Kawase, T., Olbris, D.J., Otsuna, H., Svirskas, R., and Rokicki, K. (2024). NeuronBridge: an intuitive web application for neuronal morphology search across large data sets. BMC Bioinformatics *25*. https://doi.org/10.1186/s12859-024-05732-7.
91. Moore, R.J.D., Taylor, G.J., Paulk, A.C., Pearson, T., van Swinderen, B., and Srinivasan, M.V. (2014). FicTrac: a visual method for tracking spherical motion and generating fictive animal paths. J. Neurosci. Methods *225*, 106–119.
92. Isaacson, M., Ferguson, L., Loesche, F., Ganguly, I., Chen, J., Chiu, A., Liu, J., Dickson, W., and Reiser, M. (2022). A high-speed, modular display system for diverse neuroscience applications. bioRxiv, 2022.08.02.502550. https://doi.org/10.1101/2022.08.02.502550.
93. Gouwens, N.W., and Wilson, R.I. (2009). Signal propagation in Drosophila central neurons. J. Neurosci. *29*. https://doi.org/10.1523/JNEUROSCI.0764-09.2009.
94. Maimon, G., Straw, A.D., and Dickinson, M.H. (2008). A simple vision-based algorithm for decision making in flying Drosophila. Curr. Biol. *18*. https://doi.org/10.1016/j.cub.2008.02.054.
95. Reiser, M.B., and Dickinson, M.H. (2010). Drosophila fly straight by fixating objects in the face of expanding optic flow. J. Exp. Biol. *213*. https://doi.org/10.1242/jeb.035147.
96. Bates, A.S., Manton, J.D., Jagannathan, S.R., Costa, M., Schlegel, P., Rohlfing, T., and Jefferis, G.S. (2020). The natverse, a versatile toolbox for combining and analysing neuroanatomical data. eLife. https://doi.org/10.7554/eLife.53350.
97. Dombrovski, M., Peek, M.Y., Park, J.-Y., Vaccari, A., Sumathipala, M., Morrow, C., Breads, P., Zhao, A., Kurmangaliyev, Y.Z., Sanfilippo, P., et al. (2023). Synaptic gradients transform object location to action. Nature *613*, 534–542.
98. Edelstein, A.D., Tsuchida, M.A., Amodaj, N., Pinkard, H., Vale, R.D., and Stuurman, N. (2014). Advanced methods of microscope control using μManager software. J. Biol. Methods *1*, 1.